Dust formation in type IIn supernova 2014ab

Master Thesis

Written by *Nanna Marie Baars Støvelbæk*

1st July 2021

Supervised by

Christa Gall - Associate Professor

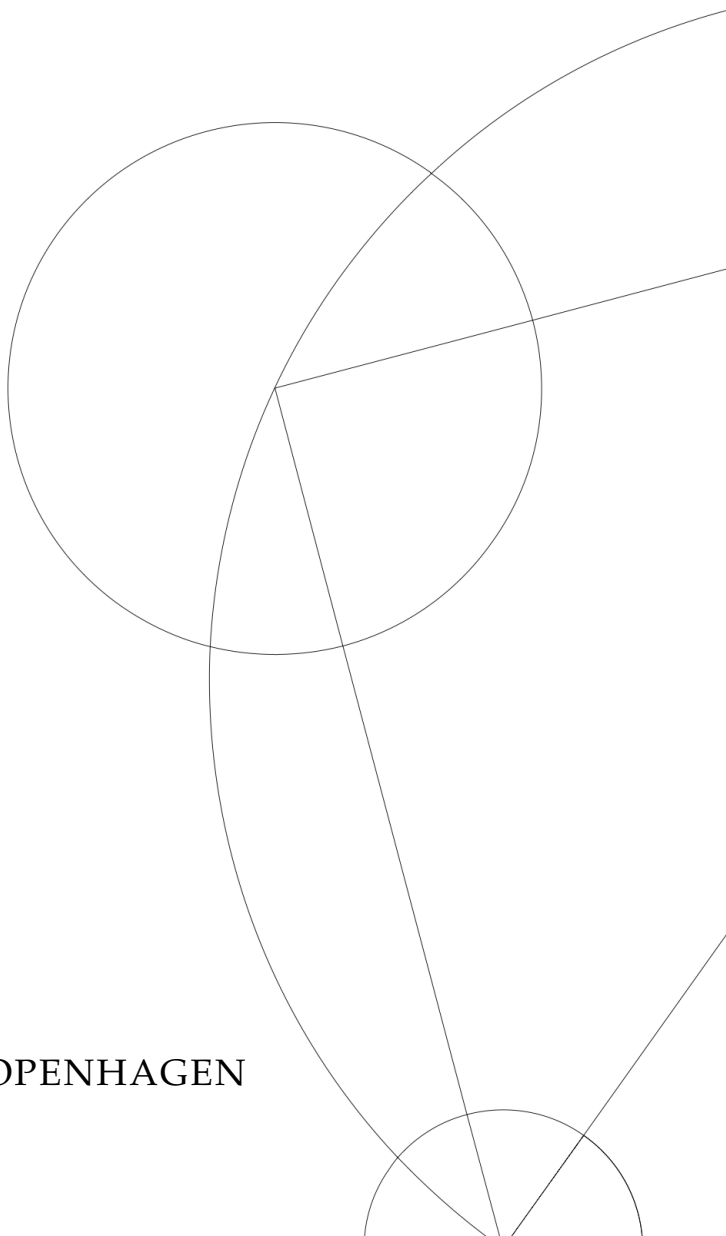

University of Copenhagen

UNIVERSITY OF COPENHAGEN

NAME OF INSTITUTE:	Niels Bohr Institute
NAME OF DEPARTMENT:	DARK
AUTHOR(S):	Nanna Marie Baars Støvelbæk
EMAIL:	vxf672@alumni.ku.dk
TITLE:	Dust formation in type IIn supernova 2014ab
SUPERVISOR(S):	Christa Gall - Associate Professor
HANDED IN:	July 1 2021
DEFENDED:	July 16 2021

NAME _____

SIGNATURE _____

DATE _____

Abstract

Core collapse supernovae (CCSNe) are known to form solids, so called dust grains, out of the elements they produce. However, the exact mechanism, timescales and quantities of this dust formation remain uncertain.
Type IIn supernovae (SNe) are suggested as playing an important role in this dust production due to the dense material surrounding the star prior to explosion, known as the circumstellar material (CSM).
In this thesis, I present my analysis of the type IIn supernova (SN) 2014ab using VLT/X-shooter spectra. Analysis of the spectra show three typical signatures of dust: 1) excess emission at near infrared (NIR) wavelengths due to thermal emission of the dust grains, 2) a blue shift of the peak of prominent emission lines, together with 3) an increasing asymmetry of the emission lines due to extinction from the dust grains.
From analysis of prominent hydrogen emission lines I quantify the dust extinction and find that the extinction is both time and wavelength dependent, which points to ongoing dust formation in SN 2014ab. Using a two component model consisting of one black body function and one modified black body function fit to the entire spectrum of each epoch, I show that there is NIR excess emission in all epochs. I find a dust temperature and mass of $T_{\rm dust} \sim 1400$ K and $M_{\rm dust} \sim 2.5 \cdot 10^4 M_{\odot}$ assuming graphite grains with a grain size of 0.1 micron. Assuming silicate grains, the dust temperature is slightly higher with $T_{\rm dust} \sim 1500$ K, and the dust mass is about a factor 10 larger than when assuming graphite grains. Assuming larger grains of about 1 micron, the dust temperature is larger and the dust mass smaller for both species.
Finally, I discuss whether my obtained results are due to pre-existing dust or ongoing dust formation, where the dust is located and how these results compare to similar SNe. I find that there is less extinction than observed in other type IIn SNe such as SN 2010jl, and I find that for SN 2014ab, the spectral signatures are more likely due to ongoing, newly forming dust than due to pre-existing dust.

Acknowledgements

First of all I would like to thank my supervisor, Christa Gall. For providing me with valuable guidance, always having time for me and her unwavering support through rough times.
Secondly I would like to thank the staff and students at DARK for including me in activities, providing me with access to many interesting talks and supporting me morally throughout this process. I would especially like to thank Zoe Ansari for providing valuable help with codes, Nikki Arendse for being my mentor and friend, providing me with help when needed and always being there to support me, and Cecilie Hede, for her support and friendship and always answering any stupid questions I might have.
I would also like to personally thank my family and friends for always believing in me, for their constant reminders that I am smart and worthy and for supporting me in any way necessary.
Last but not least I want to thank my loving husband Kevin Baars Støvelbæk. For being my biggest support, a shoulder to cry on, for going through the entire process with me and for always saying 'het komt wel goed, schatje'.

Contents

Chapter 1

Introduction

Interstellar dust is an important component of our galaxy and important to take into account when we observe the Universe. It obscures most regions in visual and ultraviolet wavelengths, and reradiates the energy in near to far infrared (IR) wavelengths, thereby also providing a large part ($\sim$ 30%) of the luminosity of the Milky Way (MW). Dust is also crucial for the formation of stars and further controls the temperature of the interstellar medium (ISM) by providing cooling as well as heating through electrons ejected from the grains. (Sluder and Milosavljević, 2018, Sarangi, Matsuura, and Micelotta, 2018).
However, current theories for dust formation are not sufficient to explain the amount of dust formed in various environments. Dust discovered at very high redshifts indicate that a fast and efficient dust production mechanism is needed. At these redshifts (z > 6) large amounts of dust ($\geq 10^8$ $M_\odot$) have been detected in sub-millimeter galaxies and quasars. Only stars of relatively high mass (> 3 $M_\odot$) are sufficiently short-lived to be potential dust sources (Gall, Hjorth, and Andersen, 2011). One of the possible sources of dust are CCSNe due to their short lifetimes and large production of metals (Gall and Hjorth, 2018). There is especially growing evidence for dust formation in type IIn SNe due to their dense and hydrogen rich CSM (Gall et al., 2014, Smith and Andrews, 2020). However, observations of nearby CCSNe reveal lower amounts of dust than those found by theoretical models (Gall, Hjorth, and Andersen, 2011).

1.1 Core-Collapse Supernovae

The evolution of stars, and how they end their lives, depends on their mass. Stars with a mass of $\leq 8M_{\odot}$ shed most of their hydrogen envelope in the form of a planetary nebula during the helium burning phase. The burned out core then settles and becomes a white dwarf. However, more massive stars ($> 8M_{\odot}$) do not pass through a planetary nebula phase and instead die in CCSN explosions.

The core of these massive stars get increasingly hotter during its aging process, igniting various stages of thermonuclear fusion. This continues until the core is converted into iron, at which point the thermonuclear fusion can no longer provide energy. The core then rapidly contracts and heats to around $5 \cdot 10^9$ K in a very short time span, within a tenth of a second.
The very hot core emits gamma-ray photons with such large energies that they cause photodisintegration of the iron nuclei that they collide with, breaking them down to smaller helium nuclei. This causes the core to become so dense that its negatively charged electrons are forced to combine with its positively charged protons, creating electrically neutral neutrons. When the density of the core exceeds the nuclear density, the contraction seizes and the innermost part of the core bounces back and expands. This bounce creates a pressure wave outward towards the outer parts of the core.
During this process, the cooling of the core has caused the pressure outside of the core to decrease extensively, thus causing the material in this region to succumb to gravity and fall inwards. This material now encounters the outward moving pressure wave causing it to move outwards again. This wave reaches speeds greater than the speed of sound in the outer layers, thus becoming a shock wave.
Within a matter of a few hours, the shock wave reaches the surface of the star, by which time the outer layers of the star have started to lift off from the core. These outer layers have thinned sufficiently to allow a portion of the energy from the shock wave to escape as light, the star has thus become a SN. (Freedman, 2014)

A SN can also form without the collapse of the core of a massive star, therefore the above described SN is defined as a CCSN.

1.1.1 CCSN Sub-types

SNe are classified based on their explosion mechanism and the elements present in their spectra (Fig. 1.1). Type II SNe are defined by the presence of hydrogen lines in the spectra, while type I SNe are defined through their absence.
CCSNe of type I are divided into 2 subtypes; type Ib which is produced by core collapse in a massive star that lost the hydrogen from its outer layers but still contains helium, and type Ic which is produced by core collapse from a massive star that lost both the hydrogen and helium from its outer layers (Freedman, 2014).

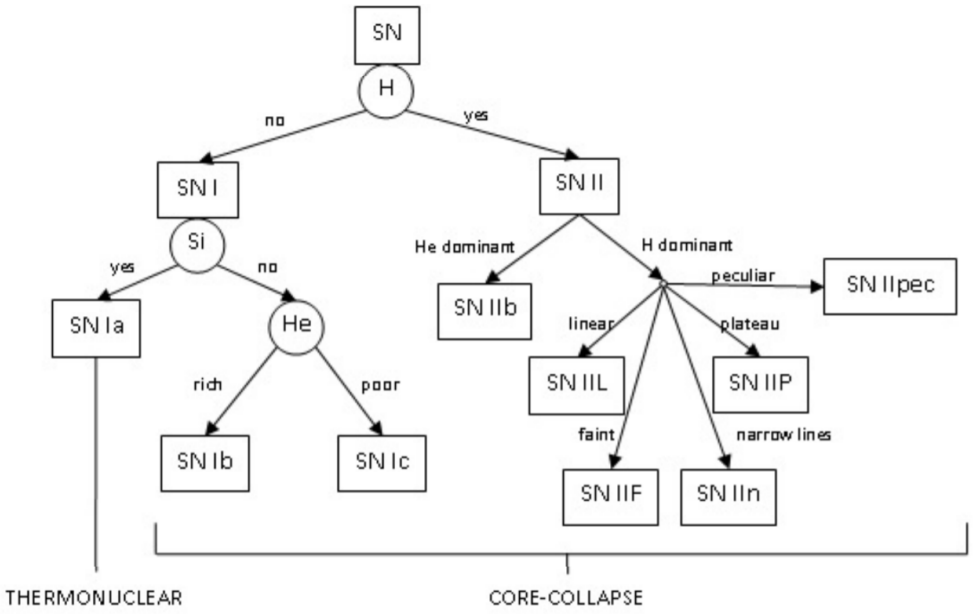

Figure 1.1: Family tree of the SN types and subtypes (Módolo, Guimarães, and Rosa, 2015)

SNe of type II occur from the death of highly evolved massive stars that still contain an abundance of hydrogen in their atmosphere at the time of the explosion. These hydrogen atoms get excited during the explosion and thus produce prominent hydrogen emission lines visible in the spectra (Freedman, 2014).
These are again divided into subtypes, named after the features of their spectra. Most prominent are:

- IIP: Where the P stands for plateau. These have a distinct plateau in their spectra (typically with a length of 50-100 days) which comes from the recombination of hydrogen.
- IIL: Where the L stands for linear. These have a more linear decline with possibly a smaller (<50 days), less distinct plateau.
- IIn: Where the n stands for narrow. These have very narrow emission lines (with widths of a few 100 km s^{-1}) coming from the unshocked CSM.

The CCSN subtypes can be roughly aligned in order of increasing progenitor mass and mass loss. However this is not due to a one-to-one correspondence between progenitor mass and spectral type, but more likely due to increasing mass-loss of the hydrogen envelope (for Type II SNe) and subsequent stripping of the helium envelope (Type I SNe) of the progenitors (Gall, Hjorth, and Andersen, 2011).

1.1.2 Type IIn SNe

SNe of type IIn are observed when the star has a shell of dense material surrounding it, known as CSM. This shell appears due to rapid and intense mass loss of the progenitor star before the SN explosion (Smith and Andrews, 2020).
Luminous Blue Variable (LBV) stars have been suggested as possible progenitors to these SNe as they are some of the only observed stars with the high wind densities required for this rapid mass loss (Smith, 2016). These stars are dominated by relatively short-lived phases of eruptive mass loss, where the star may shed large amounts of mass in a single event lasting only a few years. While some low-luminosity IIn SNe could be created by the dense and slow winds of other star types (like the most extreme Red Super Giants (RSGs) and yellow hypergiants), many observed IIn SNe are consistent with CSM that has been created by the eruptive mass loss of LBVs (Smith, 2017).

An important feature of type IIn SNe is the cold dense shell (CDS), which is the contact discontinuity between the shocked CSM and shocked ejecta where material cools, mixes via Rayleigh-Taylor instabilities, and piles up (Smith, 2016), see Fig. 1.2.
The high density allows for efficient and rapid cooling, possibly to temperatures low

enough to allow for dust formation. The rapid cooling and high density can trigger early dust formation in the CDS (Gall, Hjorth, and Andersen, 2011).

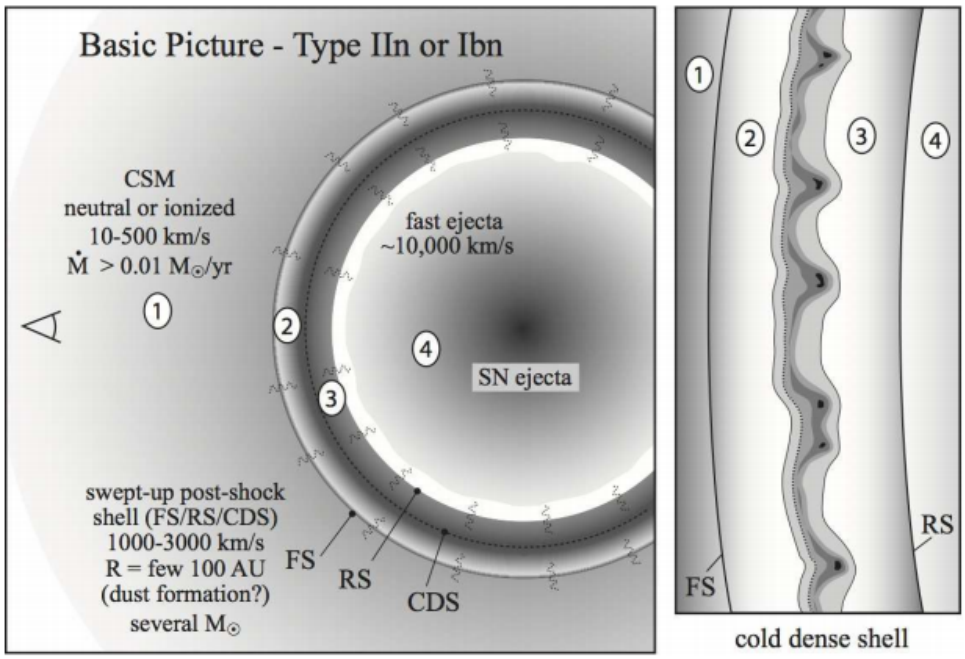

Figure 1.2: This figure illustrates the basic picture of type IIn SNe. The 4 main components are: (1) the pre-shock CSM, (2) the shocked CSM, (3) the shocked SN ejecta, and (4) the freely expanding SN ejecta. These zones are divided by the forward shock, the reverse shock and the CDS (Smith, 2016).

The most prominent emission lines typically exhibit multiple velocity components occurring from these different areas of the SN; a narrow component (full width at half maximum (FWHM) of a few hundred km s^{-1}), an intermediate component (FWHM of a few hundred to few thousand km s^{-1}) and a broad component (FWHM $\sim$ 5000-10,000 km s^{-1}.

These components occur due to different processes, a combination of SN emission and interaction with the CSM. The narrow velocity component is produced by the unshocked CSM, whereas the intermediate and broad velocity components are produced by shocked, high-velocity SN ejecta, the intermediate being the result of the collision of the ejecta with the CSM (Gall et al., 2014, Sarangi, Matsuura, and Micelotta, 2018).

1.2 Dust

Dust is formed by a series of chemical reactions where atoms/molecules from the gas phase combine into clusters that accumulate to larger and larger sizes, typically with sizes in the range of $0.001 - 0.25\mu$m for the MW (Mathis, Rumpl, and Nordsieck, 1977). Larger grains have been inferred from observation of SNe, for instance SN 2010jl where sizes up to 5 μm were found (Gall et al., 2014). The formation and growth of these dust grains thus depends on the elemental compositions of the gas phase (Gall, Hjorth, and Andersen, 2011).
Although dust only makes up $\sim$ 1% of the mass in the ISM, it is important to consider as it diminishes radiation for shorter wavelengths, can serve as a tracer of physical conditions and plays a vital role in creating structure in the Universe. The surfaces of dust grains act as chemical factories and as catalysts, creating molecules, such as H_2 (Sluder and Milosavljević, 2018, Wakelam et al., 2017).
In theory, the process of dust formation is described by two steps, the condensation of seed clusters from the gas phase and the subsequent growth to macroscopic dust grains of certain sizes and species.
The resulting dust species depends on the environment in which it is formed with predominantly either carbonaceous dust or silicates forming.
Carbonaceous dust consists mainly of carbon, with an appearance depending on the types of carbon hybrid orbitals. Other dust grains that form in carbon rich environments are the silicates, categorized as either amorphous silicates or crystalline silicates depending on their structure (Gall, Hjorth, and Andersen, 2011,Henning, 2010).

1.2.1 Supernova Dust

The discrepancy between observationally and theoretically determined dust yields has provoked a reconsideration of SN dust formation theories, and models including dust destruction have been developed. Some models demonstrate that dust grains can be effectively destroyed in a reverse shock on timescales up to $\sim 10^4$ years after the SN explosion (Bianchi and Schneider, 2007), however they are unable to explain the low observed dust masses at earlier epochs (Gall, Hjorth, and Andersen, 2011).
Other theoretical models predict that dust masses of order $10^{-1} - 1 M_{\odot}$ can form within

the first 600-1000 days (Todini and Ferrara, 2001, Nozawa et al., 2003). However, on average $10^{-4} M_{\odot}$ of relatively hot gas has been reported from observations of supernova remnants (SNR) at early epochs, while large amounts of cold dust (< 50 K) have been claimed in SNRs.
The theoretical models for SN dust formation are complicated by various complex processes that are not well understood, such as the SN explosion mechanism and subsequent expansion. As such, the amount and type of dust formed depends strongly on the assumptions made in the models (Gall, Hjorth, and Andersen, 2011).
Regardless of SN type or progenitor mass, only hot dust at low amounts, $> 3 \cdot 10^{-3} M_{\odot}$ is present at early epochs. At late epochs a large range of dust masses have been reported. One hypothesis is that, with time, dust grains grow to increasingly larger sizes, thus increasing the total amount of dust. However, another hypothesis points to the instrumental bias of only detecting hot dust at early epochs. At these epochs no observations sensitive to cold dust have been accomplished. So we cannot rule out the presence of cold dust at early epochs (Dwek et al., 2021).
Independent of the epoch of observations the amount of cold dust is significantly larger than hot dust, thus possibly yielding lower reported dust masses (Gall, Hjorth, and Andersen, 2011).

In SNe, dust forms in the freely expanding ejecta where the temperatures are low enough for formation. Here the ejecta is rapidly expanding, achieving decreasing densities, which poses a problem for dust formation since this requires high densities. Even if dust forms in the ejecta, it might get destroyed when it crosses the reverse shock. Though, as explained in section 1.1.2, in type IIn SNe evidence suggests that dust can rapidly form in the extremely dense, post-shock cooling layers (zones 2 and 3 in Fig. 1.2). As this dust is formed behind the forward shock it stands a better chance of surviving and moving into the ISM (Smith, 2016).
In order to discover ongoing dust formation in SNe there are three common observational signatures one can examine: 1) a faster decline in the optical light curve (LC), 2) an increasing excess emission at IR wavelengths from thermal emission of dust grains and 3) an increasing and wavelength dependent blue shift of the peak of prominent emission lines, together with an increasing asymmetry of the emission lines due to extinction from the dust grains (Sarangi, Matsuura, and Micelotta, 2018).

Chapter 2

My Thesis Work

The purpose of this thesis is to quantify early dust formation in SN 2014ab. This will add to the growing observational evidence that dust is indeed forming in CCSNe and that it can form even at early epochs in type IIn SNe.

In the following chapters I examine five VLT/X-shooter spectra of the type IIn SN 2014ab in order to quantify the three observational signatures described in section 1.2.1. My aim is to determine if and when dust has formed in the SN as well as quantifying the amount formed.
I will then compare my results to those found by Gall et al., 2014 with the SN 2010jl, Smith and Andrews, 2020 with the SN 2017hcc and the previous work done on SN 2014ab by Moriya et al., 2020. Lastly, I will discuss the implications of my results.

2.1 SN 2014ab: Discovery and Characteristics

SN 2014ab was first discovered by the Catalina Real-time Transient Survey (CRTS) in an image taken by the Catalina Sky Survey (CSS) on March 9.43 UT (JD-2456725.93). It was determined to be a transient with an apparent magnitude of 16.4 situated 1″5 north of its host galaxy MCG +01-35-037 at coordinates (J2000.0): RA = 13h45m05s.99 and Dec = +07deg23′16″40 (see Fig. 2.1).

On March 10.25 UT, a NIR spectrum was obtained by CSP-II, using the Folded-port Infrared Echellette (FIRE) spectrograph, which is attached to the Magellan Baade 6.5m Telescope located at Las Campanas Observatory (LCO).
The spectra revealed that the transient was a type IIn SN and it was then given the International Astronomical Union (IAU) designation of SN 2014ab. This classification was confirmed by the Public ESO Spectroscopic Survey for Transient Objects (PESSTO) by a visual spectrum taken with the New Technology Telescope located at the ESO La Silla Paranal Observatory (Moriya et al., 2020).

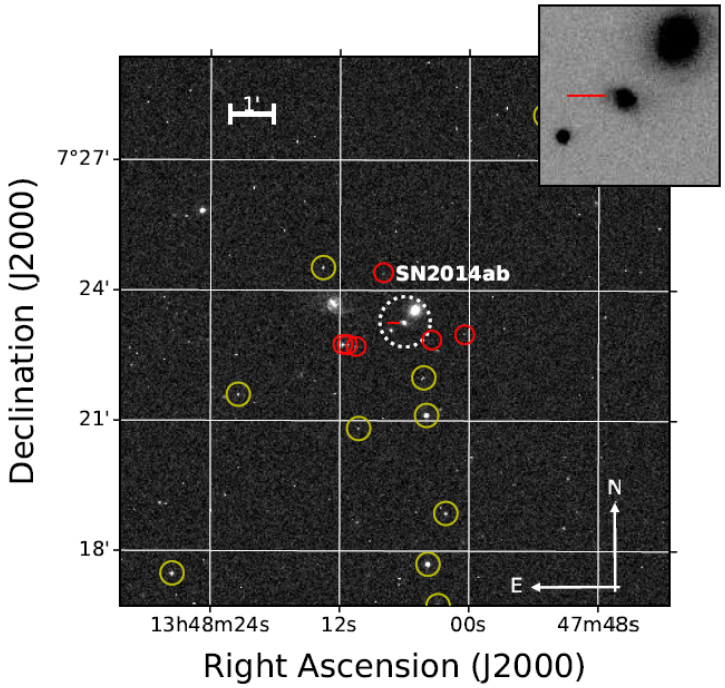

Figure 2.1: Finding chart constructed using a single *r*-band image obtained on 03 March 2014 with the Swope 1.0m telescope. The position of SN 2014ab is indicated with a dotted circle and the approximate area contained within the circle is shown in the upper right inset. Optical and NIR local sequence stars are indicated with yellow and red circles, respectively (Moriya et al., 2020).

In the NASA Extragalactic Database (NED)[1], the redshift of the host galaxy MCG +01-35-037, is given by $z = 0.02352$.

[1] `https://ned.ipac.caltech.edu/`

By examining a number of prominent, narrow emission lines of the spectra obtained with the X-shooter from the ESO La Silla Paranal Observatory's Very Large Telescope (VLT), I determined the redshift of SN 2014ab to be $z = 0.022569 \pm 0.000068$ (see section 4.1). This value is in agreement with that of Moriya et al., 2020 who found a value of $z = 0.02262 \pm 0.00001$. By assuming $H_0 = 70$ km s^{-1} and $\Omega_M = 0.27$, this redshift corresponds to a luminosity distance of 98.332982 Mpc.

In NED, the MW visual-band extinction in the direction of SN 2014ab is reported to be $A_V^{MW} = 0.083$ mag, assuming a Fitzpatrick reddening law with $R_V = 3.1$. The spectra were dereddened for MW extinction before analysis. In the following it is assumed that SN 2014ab suffers from minimal to no host-galaxy reddening.

2.2 Previous Work on SN 2014ab

This SN has previously been documented by Moriya et al., 2020 and I will here briefly bring their main results and conclusions in regards to dust formation.

Moriya et al., 2020 use the broad-band optical through mid-infrared (MIR) photometry to construct spectral energy distributions (SEDs) for each observed epoch. These are then fitted with black body (BB) functions in order to estimate the temperature, radius and luminosity profiles associated with the underlying emission regions. From this, the temperature at early epochs is determined to be $\sim$ 8000 K. In the later epochs, from 360 d and onward, Moriya et al., 2020 find that there is an excess of MIR flux present in the spectra, and those epochs are therefore fitted with an additional BB component. The second component yields a temperature of $\sim$ 2000 K, close to the dust evaporation temperature.
From examining the LC of SN 2014ab (found by integrating the BB fits) the warm component (2000 K) appears to dominate over the hot (8000 K) by 360 d. Moriya et al., 2020 suggest that the warm component is related to dust reprocessing of shorter wavelength to longer wavelength photons.

Next the spectroscopic data is examined, which will be the main focus of my thesis.

Moriya et al., 2020 find the narrow line components consistent with type IIn SNe characteristics, as well as the broad components of the hydrogen lines. These are then fitted with Lorentzian functions, giving a FWHM from Hα of 3500 km s^{-1} and a blueshift of the peak of -500 km s^{-1} (see Fig. 2.2). However, Moriya et al., 2020 conclude that this blueshift is not time or wavelength dependent as one would expect for ongoing dust formation.

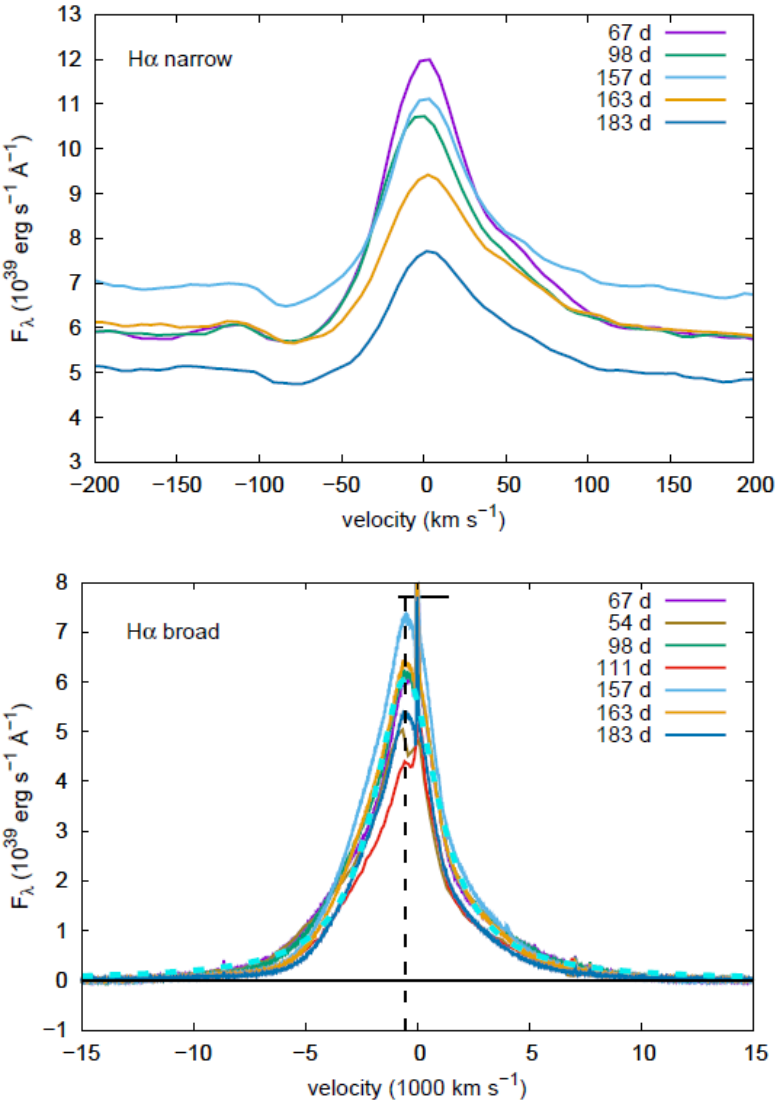

Figure 2.2: Time-evolution of the narrow and broad component Hα profiles as found by Moriya et al., 2020.

Even though the IR excess points to the existence of warm dust, since the time (or wavelength) dependence of the blueshifted peak is not observed, this cannot be due to ongoing dust formation. Moriya et al., 2020 instead explain the blueshift as due to the acceleration of the unshocked CSM by precursor photons.
Moriya et al., 2020 conclude that since SN 2014ab lacks observational features of ongoing dust formation, it indicates that the dust associated with the IR excess is not formed within the CDS, where the emission lines are formed during the early phase observations. Instead, it may originate from pre-existing dust located within the dense CSM that is heated by the SN shock or shock driven radiation.

Chapter 3

Data

Ten epochs of two-channel MIR imaging were taken of SN 2014ab by the Wide-field Infrared Survey Explorer (WISE) satellite, including W1-band measurements at 3.4 μm and W2-band measurements at 4.6μm. The first detection is at JD-2456671.59, 56 days before the first optical discovery. This photometry has been previously presented by Jiang et al., 2019 and further explored by Moriya et al., 2020.

Broad-band optical and NIR imaging was obtained by the CSP-II with facilities located at LCO. Twenty-two epochs of optical imaging was taken with the Henrietta Swope 1m telescope equipped with a direct optical camera containing an e2V CCD, while five epochs of NIR images were taken with the Irénée du Pont 2.5m telescope equipped with RetroCam.
The optical photometry extends from +56d to +485d, relative to the first WISE detection, with a gap between +140d and +360d when the SN was located behind the Sun. The NIR photometry is more limited, ranging from +56d to +121d.

Eleven epochs of optical and NIR spectra of SN 2014ab were taken by a number of different telescopes. The CSP-II obtained a single visual-wavelength spectrum with the du Pont telescope equipped with the Wide Field Re-imaging CCD Camera (WFCCD), and four epochs of NIR spectra with the Magellan Baade telescope equipped with the FIRE spectrograph. A single NTT spectrum was reported by PESSTO and lastly five epochs of optical/NIR spectra were obtained from the VLT equipped with X-shooter.

This thesis will focus on spectra from the X-shooter.
An overview of the spectroscopic observations from X-shooter can be found in Table 3.1.

Date (UT)	Modified Julian Date (MDJ)	Epoch (days)	Telescope	Instrument	Range (Å)
23 Mar 2014	56739.23	68	VLT	X-shooter	3050-24790
24 Apr 2014	56771.17	100	VLT	X-shooter	3050-24790
24 Jun 2014	56832.05	160	VLT	X-shooter	3050-24790
29 Jun 2014	56837.98	166	VLT	X-shooter	3050-24790
19 Jul 2014	56857.99	186	VLT	X-shooter	3050-24790

Table 3.1: Spectroscopic observations of SN 2014ab taken with the VLT/X-shooter. Epoch is defined as rest-frame days relative to the first *WISE* detection at MJD 56671.09.

3.1 X-shooter Spectra

In this thesis I use the 5 epochs taken by the VLT with the X-shooter instrument (see Table 3.1). I am using data that were observed and reduced in the following way.
The X-shooter spectra were obtained in nodding (ABBA) mode and underwent basic reduction steps in 'stare' mode for the UVB and VIS arms and 'nodding' mode for the NIR arm using the EsoReflex workflow. The UVB and VIS single-stare frames were combined using custom python scripts and optically extracted, slit loss corrected, and corrected for heliocentric velocity using a custom IDL program. The telluric correction was performed by using Molecfit. Finally, the flux scale of each of the one-dimensional, visual wavelength spectra were adjusted such that their synthetic colours match the more accurate broad-band colors computed from photometry (Moriya et al., 2020).

The spectra of SN 2014ab (shown in Fig. 3.1) exhibit a number of prominent emission lines, including the Balmer, Brackett and Paschen series of Hydrogen, which I will focus on in the following analysis.

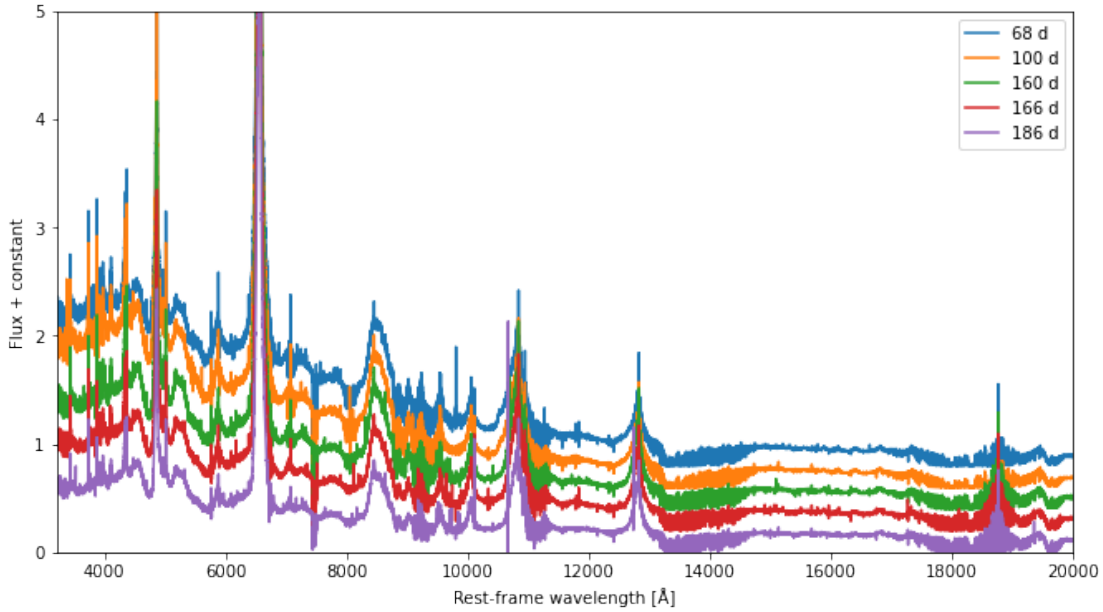

Figure 3.1: Spectra of SN 2014ab - the days refer to number of days after the first WISE detection.

All of these exhibit three velocity components: broad, intermediate and the narrow velocity component characteristic for type IIn SNe, with most of them exhibiting a narrow P Cygni profile throughout all the epochs. The intermediate velocity component results from the CDS where the forward shock is propagating through the CSM, and is where we would expect to see ongoing dust formation.

Fig. 3.2 shows the evolution of the narrow velocity component and of the full spectral line of Hα. From Fig. 3.2 we can see that the line is not perfectly symmetrical which is most likely due to the fact that the first epoch, 68 d, is recorded after peak explosion. Since all data of SN 2014ab are taken after peak, we cannot determine a specific date of explosion. I will compare the spectra and results with other known type IIn SNe in section 6.3, which might help us get a better understanding of the time frame we are looking at.

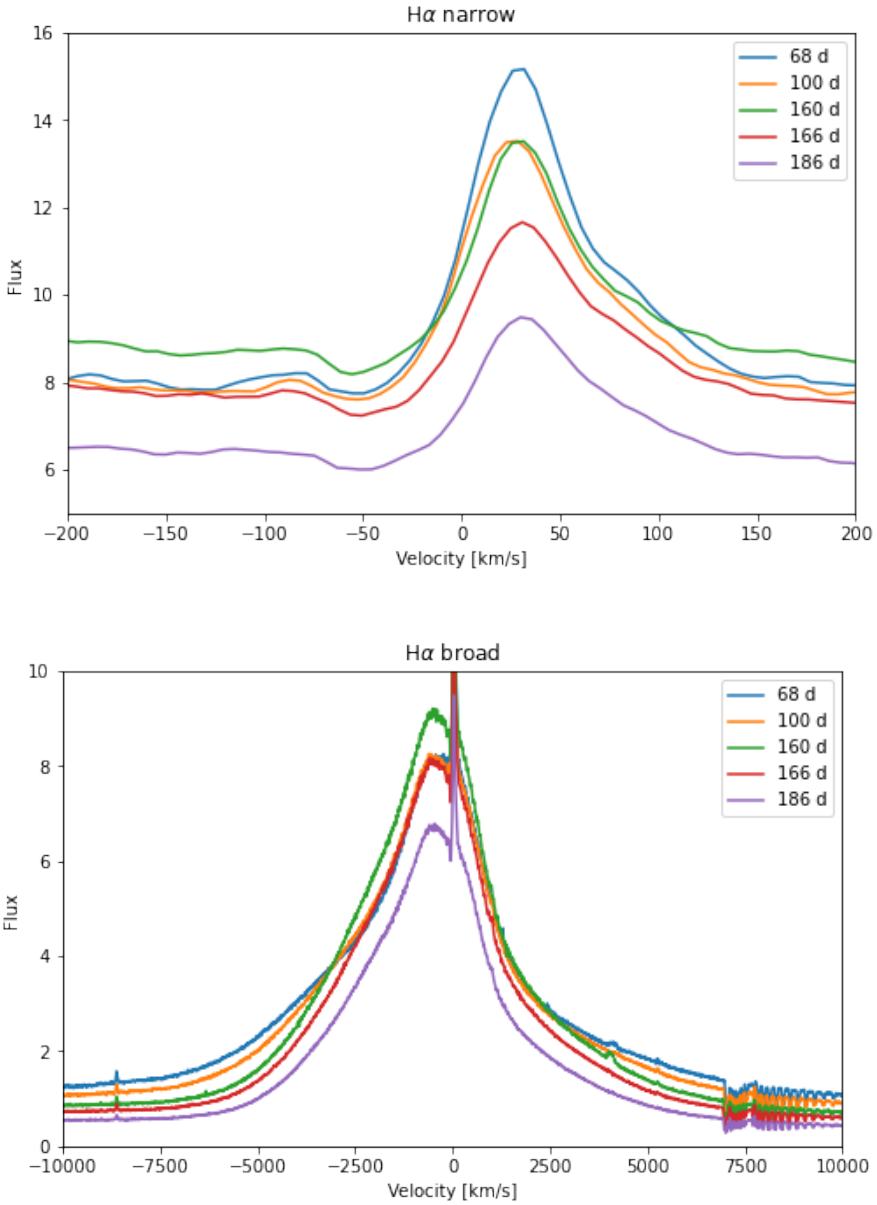

Figure 3.2: Time evolution of the narrow and broad velocity components of the Hα line profile

Chapter 4

Analysis

In this chapter I describe my analysis of the 5 epochs of VLT/X-shooter spectra. The analysis is divided into 3 key components: Lorentzian fits to spectral emission lines, calculation of extinction values and a 2 component model fitted to the entire spectra. Each of these focus on examining a specific signature of ongoing dust formation.

4.1 Preparing the Data

Prior to analysing the spectral lines, the redshift of SN 2014ab was determined using 4 prominent narrow emission lines: OIII, Hα, Hβ and Paβ. It was calculated using the formula:

$$z = \frac{\lambda - \lambda_{rest}}{\lambda_{rest}} \tag{4.1}$$

and determined to be $z = 0.022569 \pm 0.000068$. This was then subtracted from the entire wavelength range, $\lambda = \lambda_{obs}/(1+z)$, to work with the de-redshifted spectrum.

The 7 emission lines I chose to focus on in the following analysis were: Brγ, Paβ, Paδ, Hα, Hβ, Hγ and Hδ. These were translated to velocity space with the rest-frame wavelength of the line as zero velocity.
All of the spectral lines featured a narrow velocity component, with most of them featuring a P Cygni profile. A P Cygni profile consists of a broad intense emission line and a less intense absorption line. It appears in the spectra due to the large-scale motion of

material in an outflowing wind from the star (Gall et al., 2014).
As this profile makes it difficult to pinpoint the peak of the intermediate velocity component of the hydrogen lines, it was removed from each epoch of each line.

The linear background was removed from the data, by fitting a combined Lorentzian profile and linear continuum model to the intermediate velocity component. From the fit parameters, a model for the linear background was constructed and then removed from the data (see Fig. 4.1).

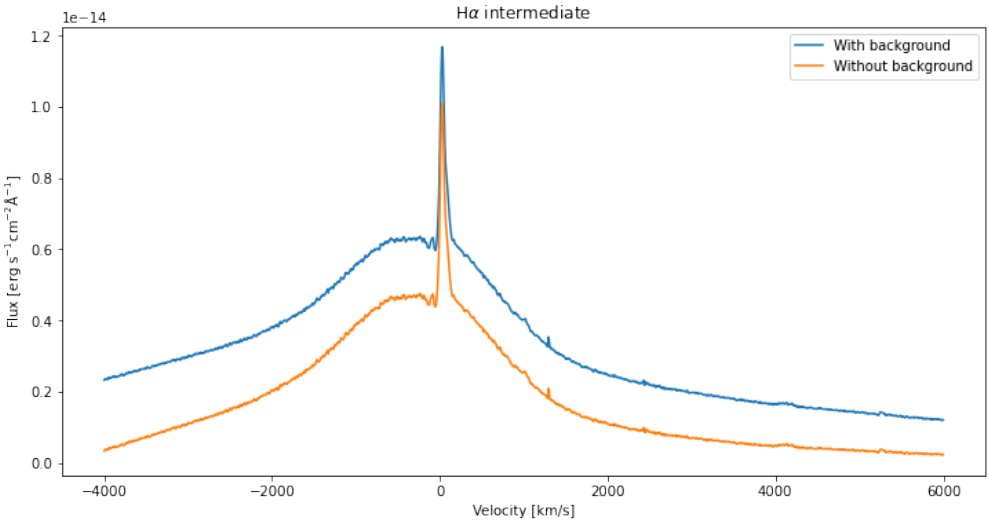

Figure 4.1: Comparison of data from epoch 1, 68 d, with and without the linear background removed.

In order to identify any evolution in the shape of the spectral lines, the flux from each epoch was normalized. This was done by taking a value on the unaffected blue side of the line, around -1000 km s^{-1}, and using this as the normalization factor (see Fig. 4.2). The blue side refers to all negative velocities and the red side is defined as all positive velocities.

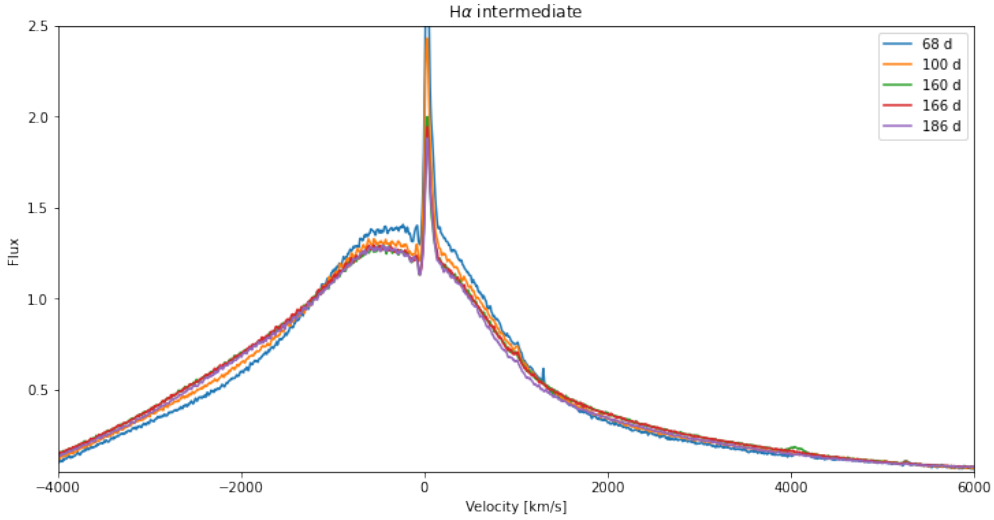

Figure 4.2: Evolution of the intermediate velocity component of Hα after normalising.

4.1.1 Signal to Noise and Contamination

The different spectral emission lines have varying degrees of signal to noise ratios (S/N). Errors from the analysis results are impacted by this variation, which becomes especially evident on IR lines that generally have a lower S/N than optical lines (see Table 4.1).

Signal to noise ratio							
	Brγ	Paβ	Paδ	Hα	Hβ	Hγ	Hδ
S/N wide	35	37	37	178	123	99	84
S/N narrow	45	51	37	209	178	119	85

Table 4.1: S/N for the spectral lines. Wide refers to the whole intermediate velocity component, used to calculate the extinction, and narrow refers to the intermediate range, used to determine blueshift.

Of the optical lines, Hδ has the lowest S/N. Apart from the high noise level there were also other aspects of this line that made the analysis difficult.

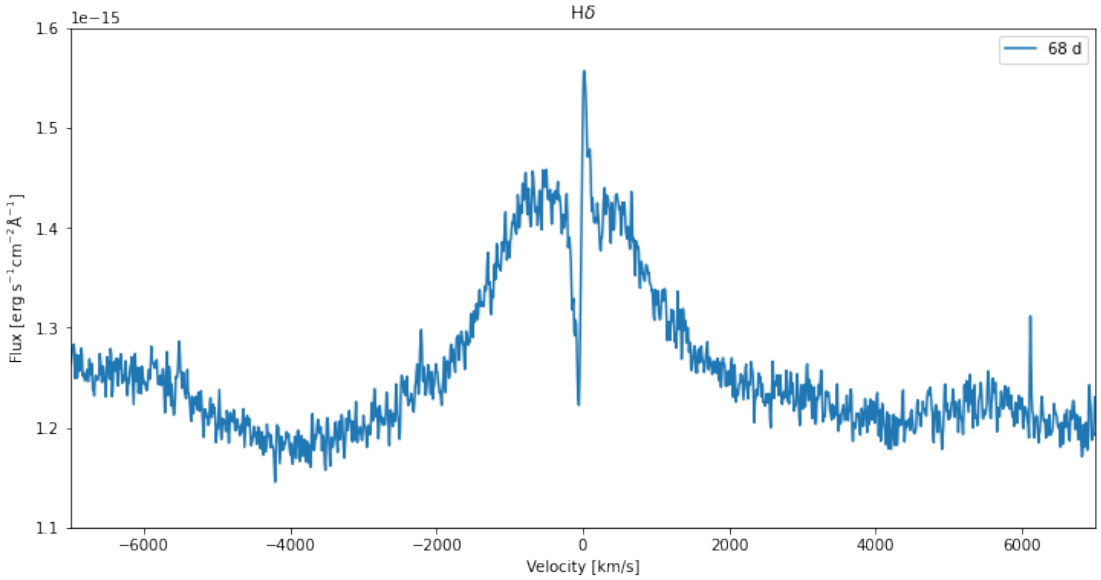

Figure 4.3: The intermediate velocity component of Hδ.

As can be seen on Fig. 4.3, Hδ has a very prominent P Cygni profile, meaning that much of it had to be removed prior to fitting. Further, this line also suffers the highest degree of extinction due to it having the smallest wavelength. Since it is most extinguished, it is also the most asymmetrical line, so therefore hardest to fit with a symmetrical Lorentzian. Finally it exhibits multiple 'bumps' on the red side of the line, seen on Fig. 4.3 at around 2500 and 5500 km s^{-1}. Since all the hydrogen lines originate from the same region we would expect all of them to have the same velocity ranges on the components. Therefore I assume that these 'bumps' are due to contamination from another line.

4.2 Line Fits

I then defined the same velocity range for each line (with the exception of Hδ and Brγ, see section 4.1.1) and fitted the intermediate velocity component with a Lorentzian profile. An attempt was made first with a Gaussian profile, but as the emission lines exhibit broad wings they were best represented by a Lorentzian.
This fit enables me to quantify the evolution of the blueshift (centroid), the FWHM from

sigma, and to constrain the parameters for the linear background. A fit on a narrow range of the intermediate velocity component was made to constrain these parameters (Fig. 4.4) and then the entire intermediate part was fitted with a Lorentzian profile for further analysis (Fig. 4.5).

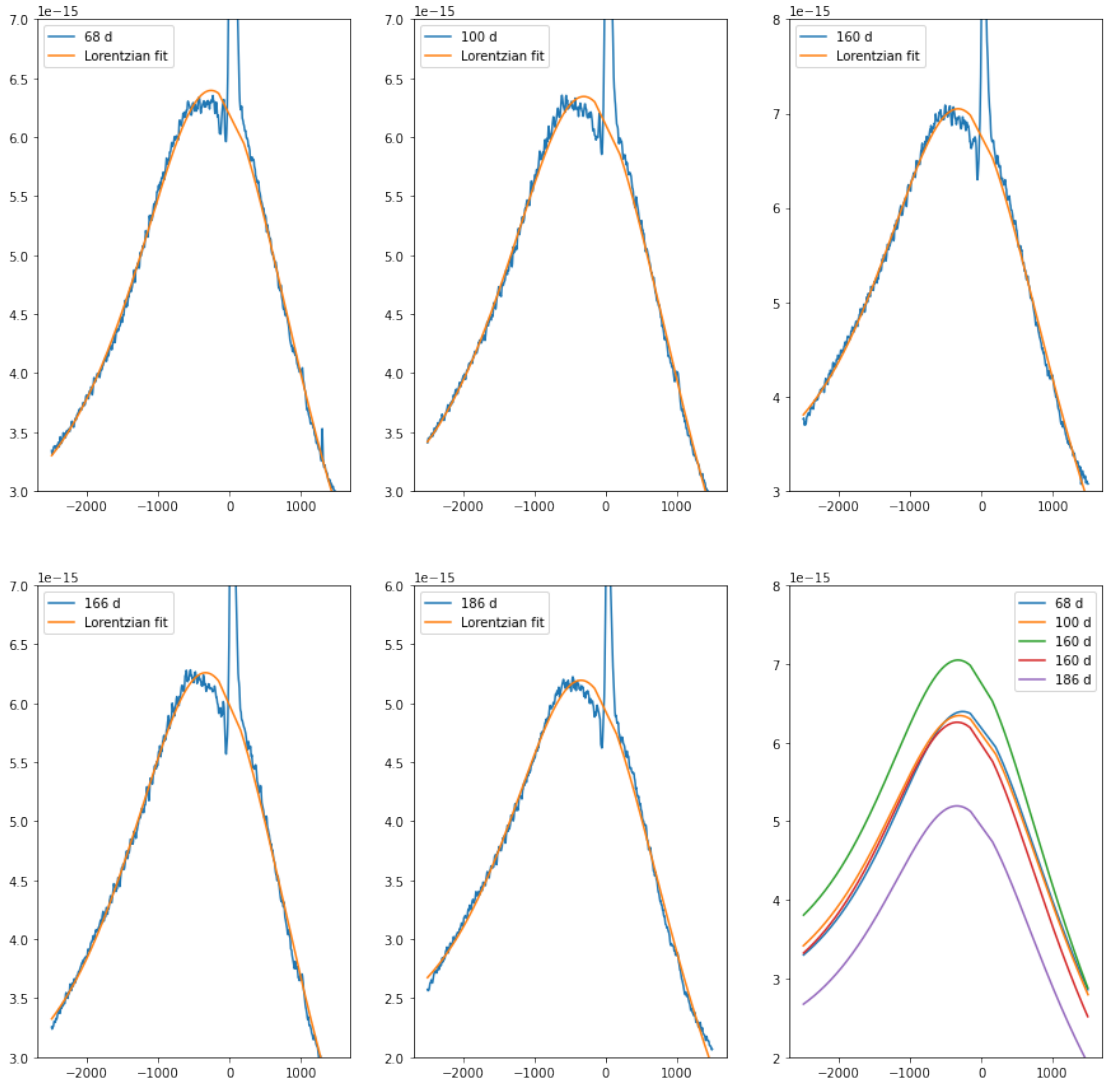

Figure 4.4: Lorentzian fits to each epoch of Hα. This fit was done on a narrow range of the intermediate velocity component to constrain the values for the blueshift and FWHM.

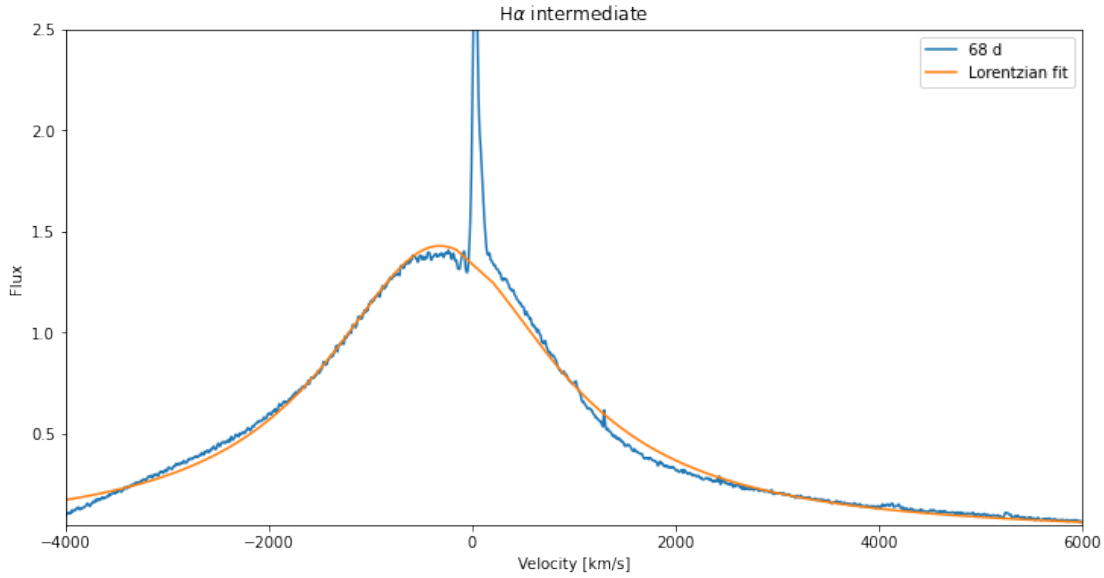

Figure 4.5: Lorentzian fit, here shown for the first epoch of Hα. This fit was done on a the full range of the intermediate velocity component to to see the evolution of the shape.

Note from Fig. 4.5 that the spectral line is slightly asymmetric already at the first epoch. This means that a perfect fit with a symmetric profile is not possible to accomplish.

4.3 Extinction

The extinction of a spectral line is based on how much of the line has been obscured by dust compared to the original line profile. As the first epoch of the spectroscopic data already exhibits some extinction (see Fig. 4.5), the intrinsic line profile (which is not affected by dust) had to be constructed.

4.3.1 Intrinsic Line Profile

In order to construct these intrinsic line profiles I used the blue, unaffected part of the lines. This part (from -4000 to 0 km s^{-1}) was cut from the spectra and mirrored around 0 km s^{-1}, the expected peak of the intrinsic profile (see Fig. 4.6).

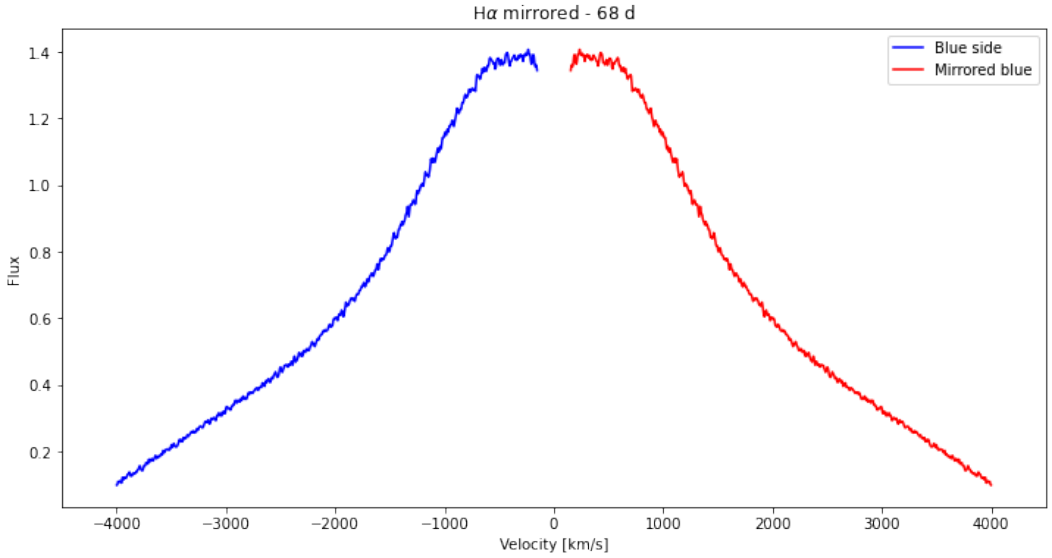

Figure 4.6: Intrinsic line profile of Hα.

This profile was then fitted with a Lorentzian profile in the same range as the intermediate line profile, as described in section 4.2. As can be seen from Fig. 4.7 below, the first epoch of the spectroscopic data already exhibits extinction.

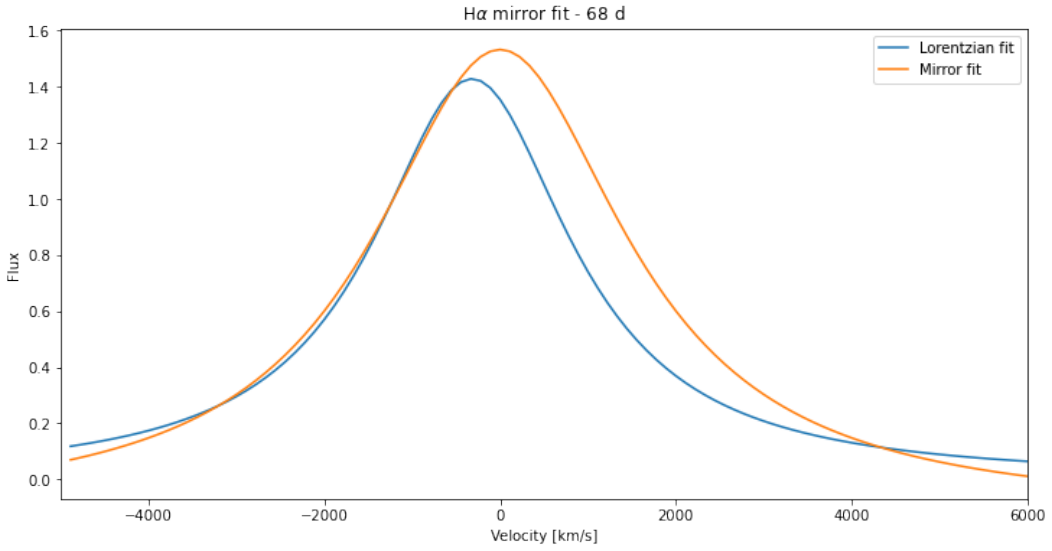

Figure 4.7: Models based on the Lorentzian fit of the intermediate velocity component and the corresponding mirror model for the intrinsic line.

4.3.2 Extinction Calculations

Using the Lorentzian fits for the line profile and corresponding mirror profile, the extinction was then calculated using the following equation:

$$A_\lambda = -2.5 \log(I(\lambda, t)/I_{ref}(\lambda)) \tag{4.2}$$

where $I(\lambda, t)$ is the integrated flux from the Lorentzian fit, and $I_{ref}(\lambda)$ is the integrated flux from the mirror fit.

Hδ was not included in the extinction calculations as most of the extinction occurs in a broader part of the intermediate velocity component, but this part is contaminated as described in section 4.1.1.

4.3.3 Errors

The errors on the extinction values were calculated using Monte Carlo simulations. The fit parameters (both for the intermediate velocity component and the mirror) were varied within their uncertainties and new extinction values were calculated for each. This was iterated over 5000 times until I acquired a distribution of extinction values for each epoch of each line (see Fig. 4.8).

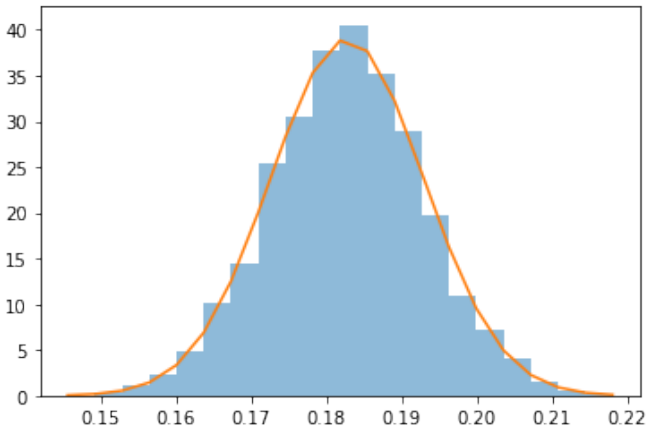

Figure 4.8: Distribution of extinction values for Hα for the first epoch.

This distribution was then fitted with a Gaussian profile which yielded the mean extinction value and standard deviation of this value.

4.3.4 Standard Extinction Laws

In order to say something about the size of the formed dust grains, the extinction curve was fitted with a Cardelli and Fitzpatrick extinction law (Cardelli, Clayton, and Mathis, 1989, Fitzpatrick and Massa, 2005). Both extinction laws use parameterized extinction data, and depend on only one parameter, $R_V = A(V)/E(B-V)$. For the MW, this parameter has an average value of $R_V = 3.1$. The inferred value for SN 2014ab thus tells us if the grains formed in SN 2014ab are larger or smaller in size than the average distribution in the MW.
However, as seen in Fig. 4.9, a simple extinction law is not enough to account for the extinction in the NIR lines. The extinction curves were therefore instead fitted with a combined model:

$$A_\lambda = A_{\text{MW}} + A_{\text{gray}} \tag{4.3}$$

where A_{MW} is a Cardelli or Fitzpatrick with the average values for the MW, and A_{gray} is an offset for the gray dust. This fit yields values for the offset and the corresponding R_V is then calculated.

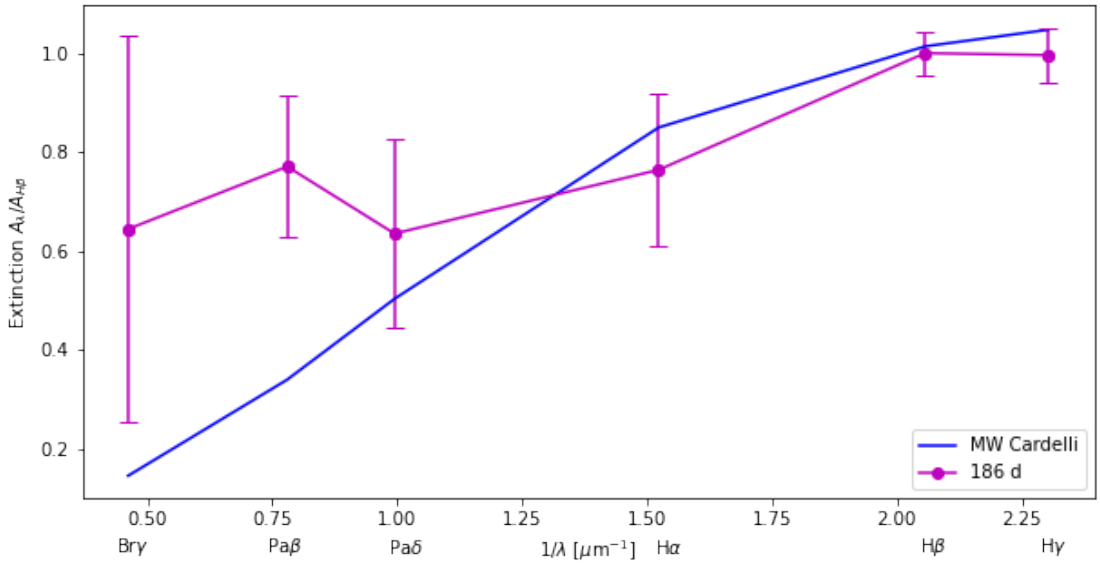

Figure 4.9: Cardelli extinction law fitted to the extinction curve of 186 d. Without the contribution from gray dust it is impossible to fit the NIR extinction values.

4.4 Modified Black Body

Next I examined the temporal evolution of the full spectra (see Fig. 4.10) to look for the characteristic IR excess. In the case of SN 2014ab, only the optical to NIR part of the spectrum is covered by the observations.

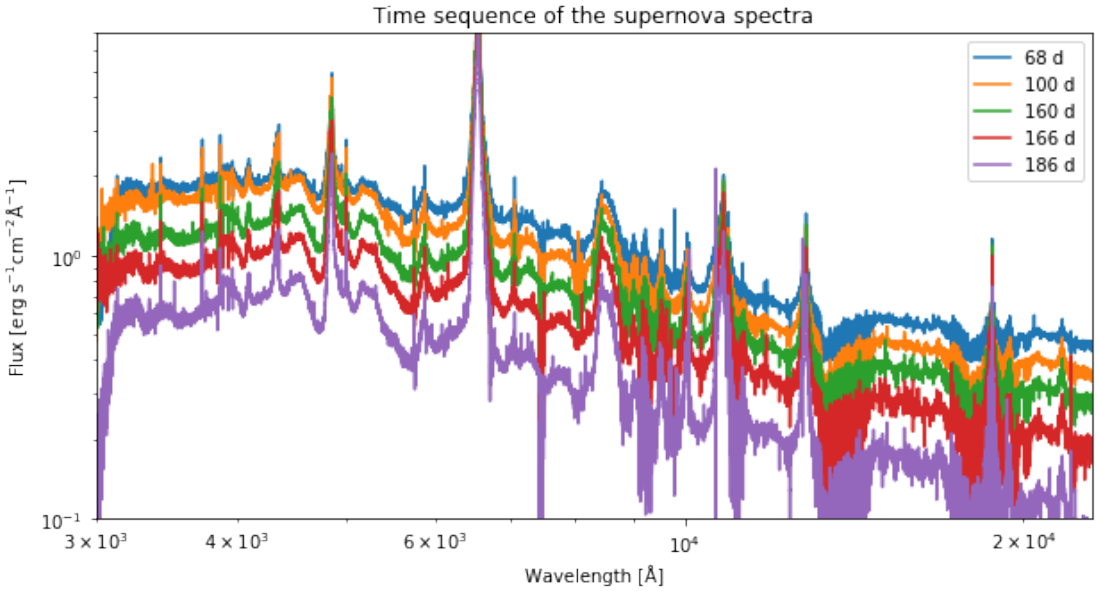

Figure 4.10: Temporal evolution of the full spectra of SN 2014ab.

The full spectra were fitted with a two component model consisting of a black body (representing the hot SN component) and a modified black body (representing the warm dust component):

$$BB_{SN}(\lambda) = \frac{2hc^2/\lambda^5}{\exp(hc/\lambda kT_{SN}) - 1} \cdot \pi \frac{R_{SN}^2}{LDS^2} \tag{4.4}$$

$$BB_{dust}(\lambda) = \frac{2hc^2/\lambda^5}{\exp(hc/\lambda kT_{dust}) - 1} \cdot \kappa(\lambda) \frac{M_{dust}}{LDS^2} \tag{4.5}$$

Combined model:

$$BB_{model}(\lambda) = BB_{SN} + BB_{dust} \tag{4.6}$$

Where h is Planck's constant, c is the speed of light, k is Boltzmann's constant, LDS is the luminosity distance and λ is the wavelength. $\kappa(\lambda)$ is the dust mass absorption

coefficient for an assumed dust species and grain size (Li and Draine, 2001, Rouleau and Martin, 1991).

The composite model yields results for the SN temperature, T_{SN}, SN radius, R_{SN}, dust temperature, T_{dust}, and the dust mass, M_{dust}. As it assumes a dust species and grain size, the model was tested for two different species, graphite and silicates, and two different grain sizes for each, 1 μm and 0.1 μm.

For the fitting, the strong emission lines and telluric regions were excluded. Fig. 4.11 shows an example of the fitted region, assuming graphite with a grain size of 0.1 μm.

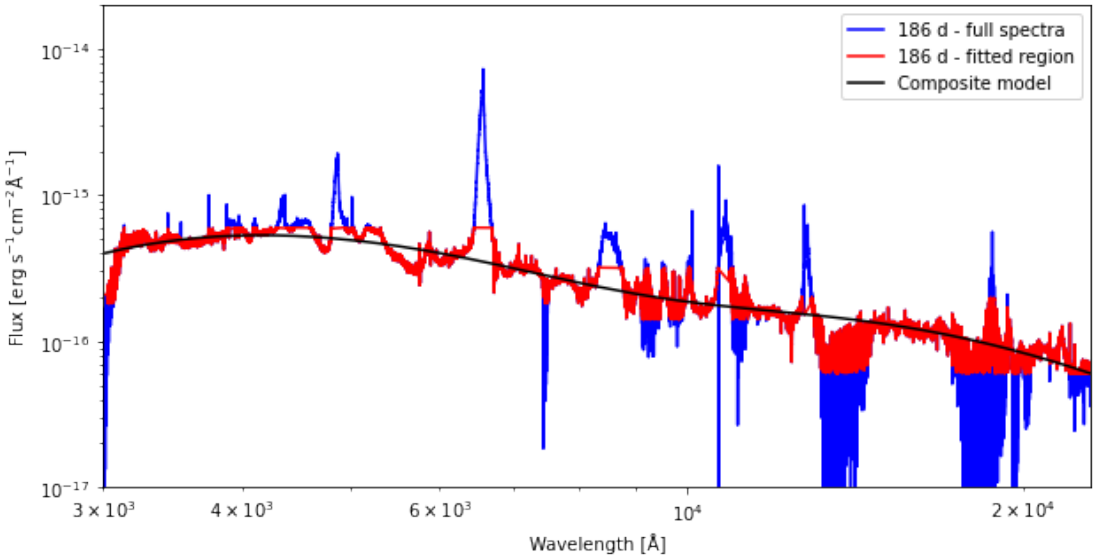

Figure 4.11: Composite model fitted for 186 d. Here assuming graphite 0.1 μm.

Chapter 5

Results

In this chapter, I present the results of the analysis described in Chapter 4. These results will be further discussed and compared to similar type IIn SNe, SN 2010jl (Gall et al., 2014) and SN 2017hcc (Smith and Andrews, 2020), in Chapter 6.

5.1 Line Fits

Each spectral line was fitted with a Lorentzian profile as described in section 4.2. This was done in a small range of the intermediate velocity component to establish the FWHM and blueshift of the peak of the spectral lines. Table 5.1 shows the temporal evolution of the blueshift for each of these lines.

	Blueshift [km s^{-1}]				
Line	68 d	100 d	160 d	166 d	186 d
Brγ	188.9 ± 36.1	295.9 ± 23.7	300.6 ± 25.5	319.6 ± 27.7	363.2 ± 23.5
Paβ	267.1 ± 15.5	323.0 ± 18.9	394.9 ± 9.7	401.8 ± 7.6	431.9 ± 8.1
Paδ	198.5 ± 10.3	341.4 ± 10.3	324.3 ± 10.1	352.3 ± 11.1	331.0 ± 10.4
Hα	186.8 ± 3.4	212.9 ± 4.1	229.3 ± 3.9	246.1 ± 3.8	254.8 ± 4.0
Hβ	227.0 ± 14.8	275.1 ± 12.1	271.4 ± 8.6	278.8 ± 10.4	294.7 ± 7.9
Hγ	243.5 ± 9.8	286.5 ± 9.1	306.5 ± 8.1	316.5 ± 8.0	349.9 ± 8.6
Hδ	222.7 ± 25.7	237.6 ± 19.1	274.7 ± 19.0	297.0 ± 16.0	373.7 ± 16.5

Table 5.1: Blueshift of the peak from the Lorentzian fits to the intermediate velocity component.

From Fig. 5.1 we can see that this blueshift is time dependent, increasing with epoch, and (somewhat)wavelength dependent, with lines at larger wavelengths getting more extinguished. This is characteristic for ongoing dust formation as explained in chapter 1. The wavelength dependence is most noticeable in the optical lines but overall is difficult to distinguish from the figure alone.
We do see large errors on some of the lines, in particular Hδ and the three IR lines, but as explained in section 4.1.1 this is due to the low S/N on these lines and possible contamination due to other emission/absorption lines in these spectral regions.
As mentioned in the analysis, we see a blueshift already at the first epoch. Since we are trying to fit a symmetric function on an asymmetric profile we should also expect to see large errors, especially for the highly affected lines. However this does point towards some dust formation already at 68 d in SN 2014ab.

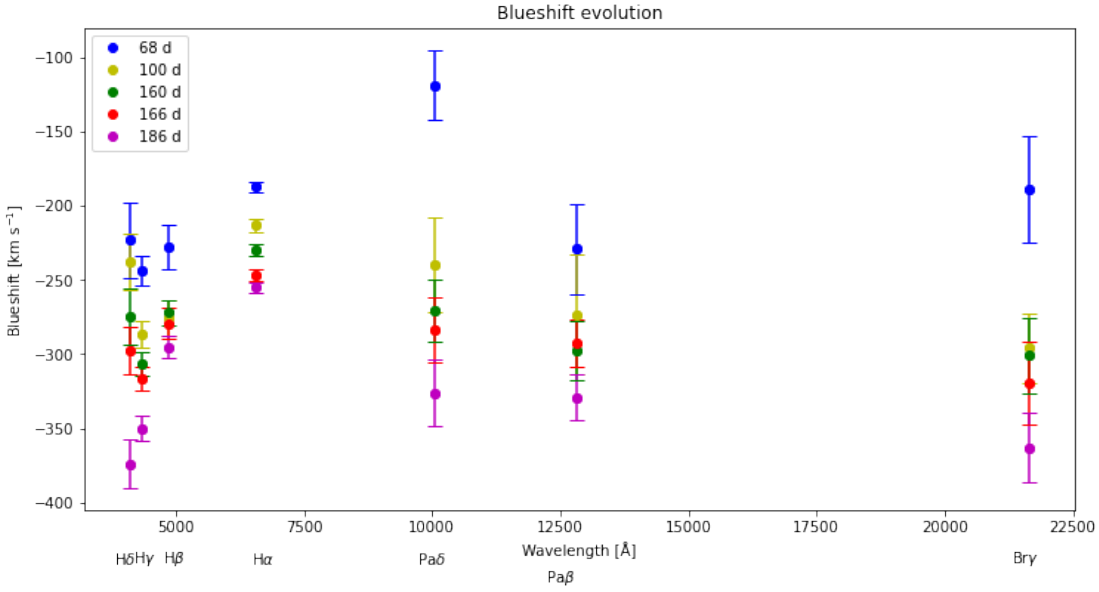

Figure 5.1: Evolution of the blueshift measured from Lorentzian fits of each epoch.

The FWHM of the lines also exhibit a time dependent evolution, decreasing with epoch. For the values of FWHM see Table A.1 and Fig. A.1 in the Appendix.
The FWHM suffers from larger errors than the blueshift due to having been found from a small range of the intermediate fit, thus not representing the whole intermediate velocity component. However, regardless of the large errors we do see a decrease in

FWHM from 68 d to 186 d across all the spectral lines.
This is another sign of dust formation as we observe more and more of the lines being extinguished by dust.

5.2 Extinction

From the constructed intrinsic line profile and the Lorentzian fits to the whole intermediate velocity component, the extinction for each line was calculated.
Table 5.2 shows the extinction values calculated from Eq. (4.2) with the corresponding errors found by Monte Carlo simulation.

	Extinction A_λ				
Line	68 d	100 d	160 d	166 d	186 d
Brγ	0.128 ± 0.096	0.180 ± 0.083	0.169 ± 0.100	0.166 ± 0.133	0.176 ± 0.107
Paβ	0.159 ± 0.063	0.172 ± 0.080	0.189 ± 0.048	0.186 ± 0.040	0.210 ± 0.039
Paδ	0.102 ± 0.063	0.164 ± 0.062	0.173 ± 0.059	0.187 ± 0.070	0.173 ± 0.052
Hα	0.191 ± 0.010	0.200 ± 0.013	0.199 ± 0.016	0.205 ± 0.015	0.215 ± 0.015
Hβ	0.233 ± 0.013	0.242 ± 0.013	0.246 ± 0.013	0.258 ± 0.014	0.273 ± 0.012
Hγ	0.212 ± 0.017	0.219 ± 0.017	0.226 ± 0.017	0.233 ± 0.015	0.271 ± 0.015

Table 5.2: Evolution of the extinction of each spectral line.

From Fig. 5.2 we can see that each spectral line gets increasingly extinguished as we move into the later epochs, but also that the line has already suffered some extinction in the first epoch, 68 d.
This extinction also exhibits the wavelength dependency that we expect from dust, that the shorter wavelength lines gets more extinguished. This is, in part, due to the fact that dust mainly absorbs light with wavelengths around the size of the dust grains. As there is an excess of smaller grains, we see more extinction from the shorter wavelength lines. As with the blueshift, the wavelength dependency is not very prominent, possibly due to the large uncertainties.

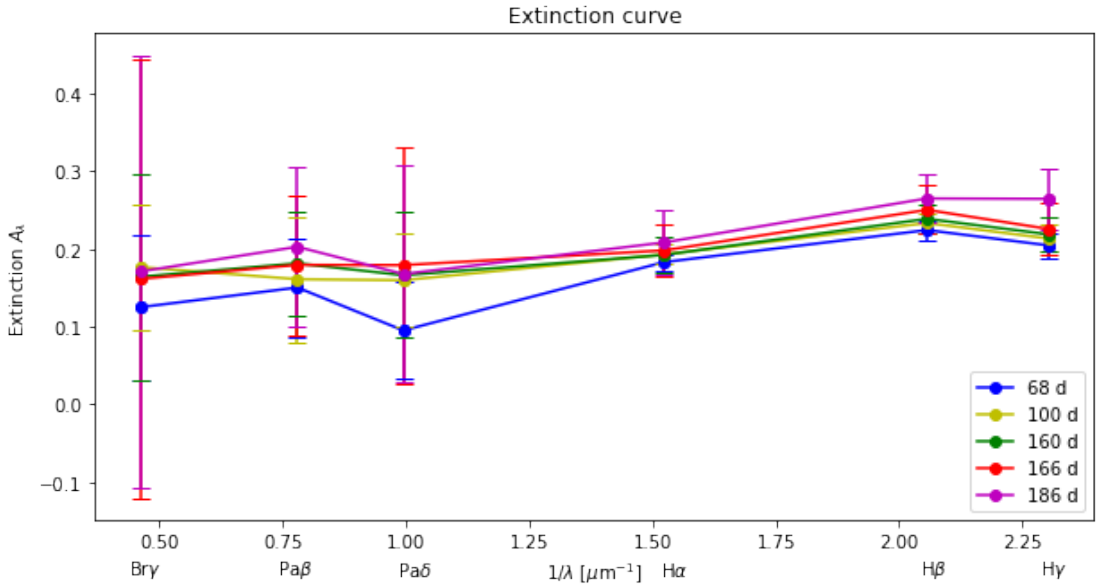

Figure 5.2: Evolution of extinction values for the different lines.

Fig. 5.2 exhibits the somewhat linear relationship between the lines as we expect from standard extinction models. There is, however, less extinction found for Hγ than expected. This could be due to the fact that we are observing at epochs too early for the line to have fully formed.
Again the three IR lines exhibit very large errors due to their low S/N.

5.2.1 Standard Extinction Laws

Fig. 5.3 shows the extinction curve fitted for the offset due to gray dust, A_{gray}. The fitting is done for both a standard Cardelli and Fitzpatrick extinction law (Cardelli, Clayton, and Mathis, 1989, Fitzpatrick and Massa, 2005). These fits both yield an offset of $A_{\text{gray}} \sim 0.5$, meaning that there is a 50 % contribution of gray dust to the extinction of Hβ (as all values were normalized to this line). What this means is that a large fraction (50 %) of the extinction is not wavelength dependent, which could imply that this fraction consist of large grains.

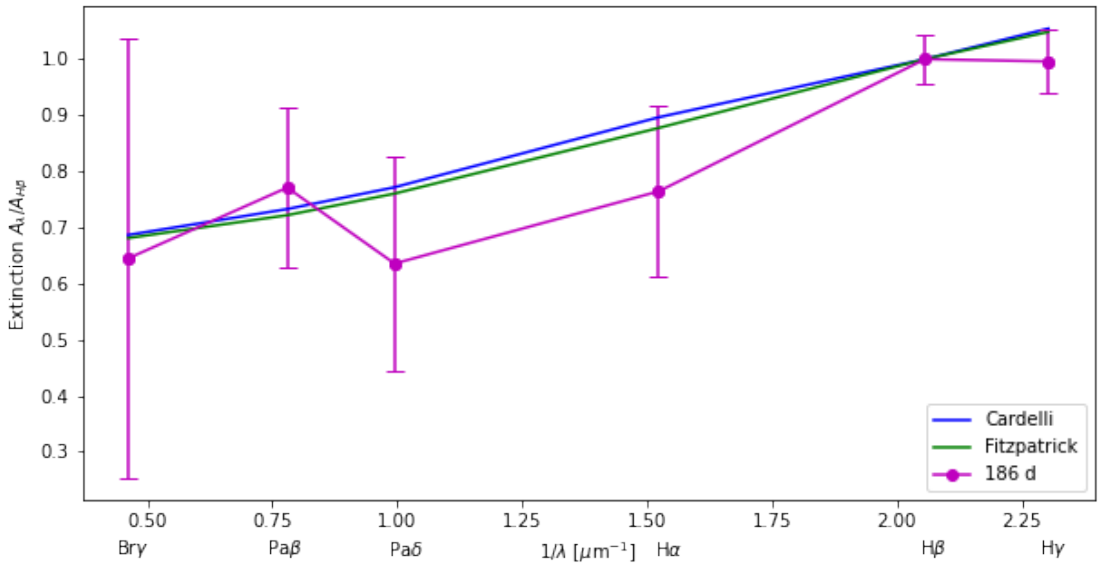

Figure 5.3: Extinction curve fitted with a Cardelli and Fitzpatrick extinction law plus an offset due to gray dust, here shown for the last epoch. All values are normalized to Hβ.

From this offset, the values of R_V were calculated for both Cardelli and Fitzpatrick. Both yielded values of $R_V \sim 8$ for 186 d. This also points to a dust composition with more large grains than for the average MW dust composition.

5.3 Modified Black Body

The entire spectrum for each epoch was fit with a composite model consisting of a BB (representing the hot SN component) and a modified BB (representing the warm dust component).
Table 5.3 and 5.4 show the parameters from the two component fit for 0.1μm graphite and silicate grains. For the results using larger grain sizes see Table A.2 and A.3 in the Appendix.

Composite model				
Epoch	T_{SN} [K]	$R_{SN} \cdot 10^{15}$ [cm]	T_{dust} [K]	$M_{dust} \cdot 10^{-4}$ [$M_\odot$]
68 d	7000.59±3.49	2.29±0.003	1474.84±15.76	0.64±0.05
100 d	7249.54±4.13	2.04±0.003	1498.09±14.19	0.68±0.05
160 d	7054.59±4.14	1.91±0.003	1323.93±7.90	2.27±0.11
166 d	7070.91±3.78	1.71±0.002	1391.13±4.55	2.32±0.05
186 d	6970.47±4.25	1.52±0.002	1382.22±3.54	2.53±0.05

Table 5.3: Evolution of fit parameters for a model assuming graphite 0.1 μm.

Composite model				
Epoch	T_{SN} [K]	$R_{SN} \cdot 10^{15}$ [cm]	T_{dust} [K]	$M_{dust} \cdot 10^{-4}$ [$M_\odot$]
68 d	7000.22±3.51	2.29±0.003	1499.79±191.81	0.99±0.79
100 d	7206.63±4.24	2.07±0.003	1568.61±326.81	0.83±0.47
160 d	7071.00±4.42	1.90±0.003	1526.54±9.69	16.78±0.68
166 d	7104.80±4.12	1.69±0.002	1613.46±5.62	14.73±0.32
186 d	7006.18±4.60	1.50±0.002	1583.19±4.38	17.77±0.31

Table 5.4: Evolution of fit parameters for a model assuming silicate 0.1 μm.

As explained in section 4.4, the composite model was tested with two different grain species, graphite and silicate, and each of those with two different grain sizes, 1 and 0.1 μm. Overall I find that the smaller grain size yields a smoother fit on the modified BB and smaller errors on the fit parameters.

Both species yield a temperature for the SN component of $\sim$ 7000 K and a radius for the SN of $\sim 2 \cdot 10^{15}$ cm.
However where they differ is on the parameters for the dust component. When assuming graphite, the model yields a slightly smaller dust temperature, and smaller dust mass by a factor of ten than when using silicates.
For a more comprehensive discussion on the implications of this see section 6.3.

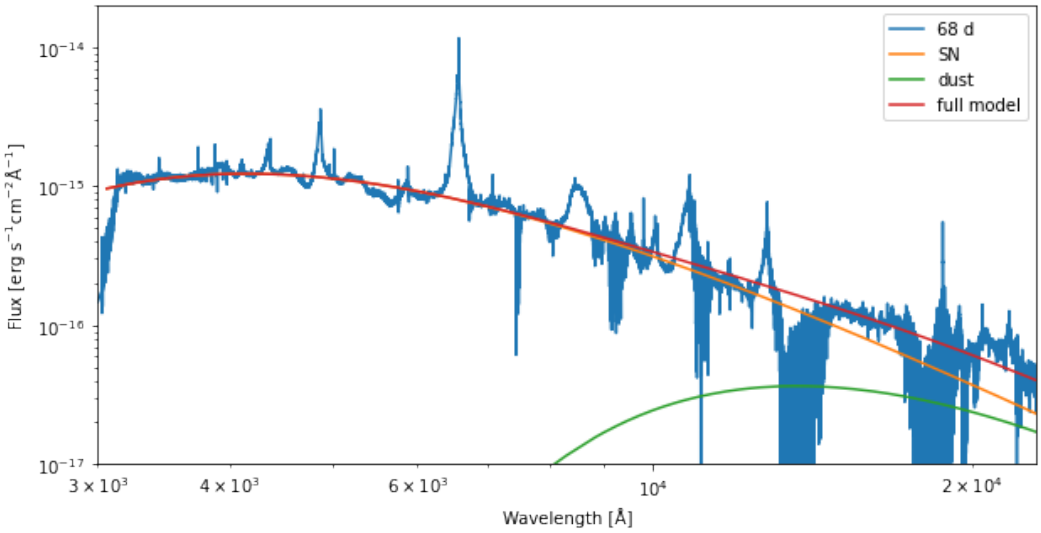

(a) Composite model for the first epoch, assuming graphite 0.1 μm.

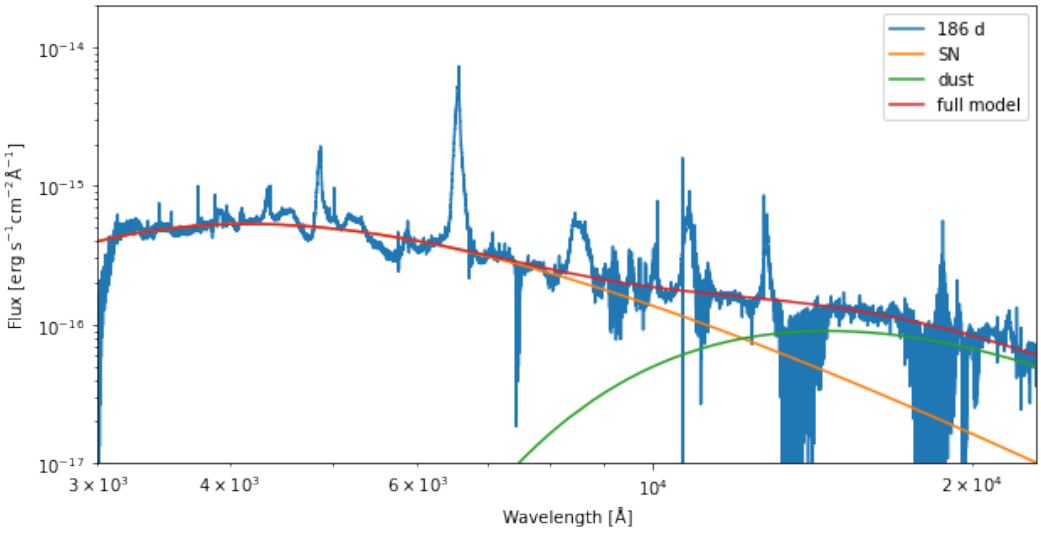

(b) Composite model for the last epoch, assuming graphite 0.1 μm.

From Fig. 5.4a and 5.4b it is evident that there is an increasing NIR excess for the later epochs. This is yet another signature of ongoing dust formation in SN 2014ab.
Note that due to the small amount of dust formed at moderately high temperatures, there is only weak dust emission at the earliest epochs, which combined with the complexity of the spectra lead to less precise fits and larger uncertainties on $T_{\rm dust}$ and $M_{\rm dust}$.

Chapter 6

Discussion

All of the results shown above indicate that there is indeed dust present in SN 2014ab. However there are still a lot of questions to be answered. Are these signatures from pre-existing or from newly formed dust? Where in the SN is this dust located? What dust species are forming and what are their sizes? How do these results compare to those of other type IIn SNe? And finally, why are the results of this thesis pointing to dust formation when the results of Moriya et al., 2020 did not?
These questions will be, if not answered then discussed in the following chapter.

6.1 Ongoing Dust Formation

Moriya et al., 2020 concluded that the dust giving rise to the IR excess was pre-existing, and that there is no ongoing dust formation in SN 2014ab. However, while pre-existing dust in the CSM can result in an IR echo when illuminated by the SN, it cannot produce the blueshifted asymmetry. If we had pre-existing dust, both sides of the spectral lines would be affected by extinction and not only the red side. From my findings I see that the blue side is more or less stable (so we might have some pre-existing dust), but that the red side gets increasingly extinguished with epoch. This characteristic point towards the formation of new dust (Smith and Andrews, 2020).

Now lets take a look at where this new dust is located. Is it in the pre-shock CSM, the SN ejecta or the post-shock CDS? The answer to this can be found by looking at the extinction from the different components of the spectral lines.
From section 5.1 we see that there is a clear evolution of blueshift coming from the intermediate velocity component of the spectral lines. However, from visual inspection of the emission lines, it appears that we also see a blueshift and extinction from the broad component, although this is smaller. This points to the fact that dust is mainly forming in the CDS but with a small amount forming in the ejecta itself (Smith and Andrews, 2020).

6.2 Dust Mass and Grain Sizes

Now that we have established that the dust is formed in the SN, we need to address the question of the type and size of this dust.

As mentioned in section 5.3, the composite model favored grain sizes of 0.1 μm over those of 1 μm. However, as mentioned in 5.2, the inferred R_V indicates a bigger fraction of large grains than for the average MW grain distribution. A more precise value for the sizes would require a more complex composite model that depends on a distribution of grain sizes.
Regarding the dust species, two different ones (graphite and silicate) were tested with the composite model. However, there is no difference in the goodness of the fit from either species. What does differ with the species is the amount of dust formed. I measure about 10 times more dust when using silicates than when using graphite. This is due to the absorption coefficient, which also differs by a factor of 10 between the two species. Silicates are more transparent than graphites and thus require a larger amount to produce the dust emission I observe in the spectra.
In reality it is likely that the dust is composed of a combination of the two species (and possibly even other species) and it is not under the scope of this thesis to accurately determine which species is the best as we miss any decisive characteristics that could tell different species apart. The current available data set it insufficient and longer wavelength data would be required. For instance, observing the prominent silicon signature

around 10-12 μm could tell if silicate dust is present in SN 2014ab. However what I can say is that the amount of dust formed with graphite seems to be in better agreement with the amounts found in other studies of type IIn SNe, see Fig. 6.1 (Gall et al., 2014,Bevan et al., 2020). Theories for dust formation also suggests a preference for carbon grains in hydrogen rich environments (Sarangi, Matsuura, and Micelotta, 2018).

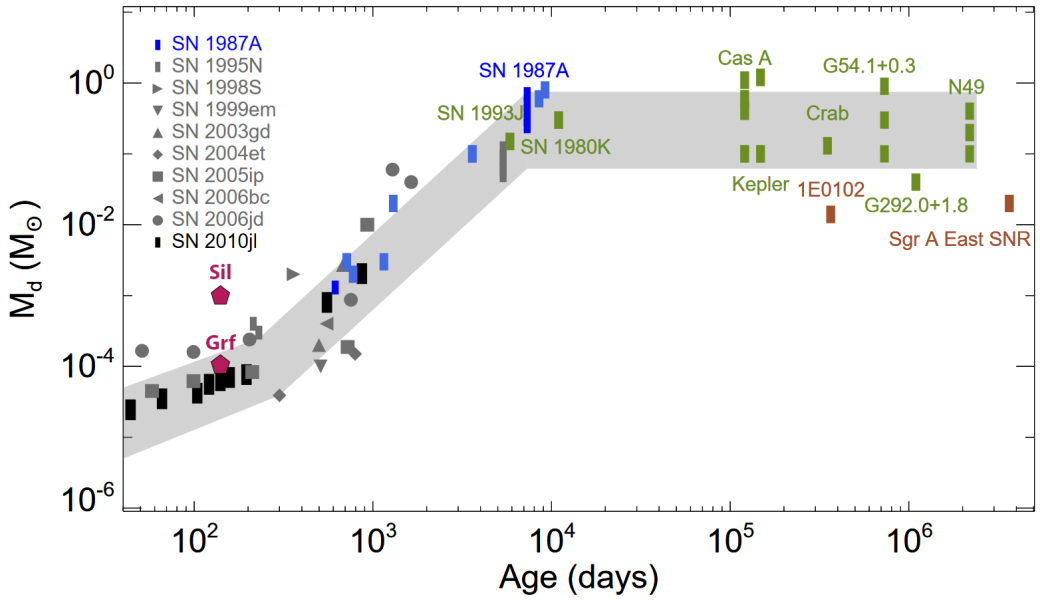

Figure 6.1: Comparison of dust mass estimates with other type IIn SNe. The pink pentagons are $M_{\rm dust}$ values for SN 2014 186 d assuming graphite and silicate 0.1 μm. Note that the age is an estimate as the exact age of this epoch is unknown. However, the value for graphite is in better agreement with the trend than that of silicate. Figure taken from Gall and Hjorth, 2018

6.3 Comparison

Now I want to examine how my results compare to other type IIn SNe.
This comparison has two goals: first of all to see how my extinction values compare with the ones found in SN 2010jl (Gall et al., 2014) and SN 2017hcc (Smith and Andrews, 2020), and secondly to compare the spectra with that of SN 2010jl in order to say something about the explosion date of SN 2014ab.

6.3.1 Spectra

The explosion date of SN 2014ab is not known and as such it is difficult to be able to say how 'early' or 'late' the dust is forming. Therefore I compare the optical spectrum of the first epoch, 68 d, with that of SN 2010jl (see Fig. 6.2). This was also done by Moriya et al., 2020 who determined that the spectrum matched that of 104 d for SN 2010jl.

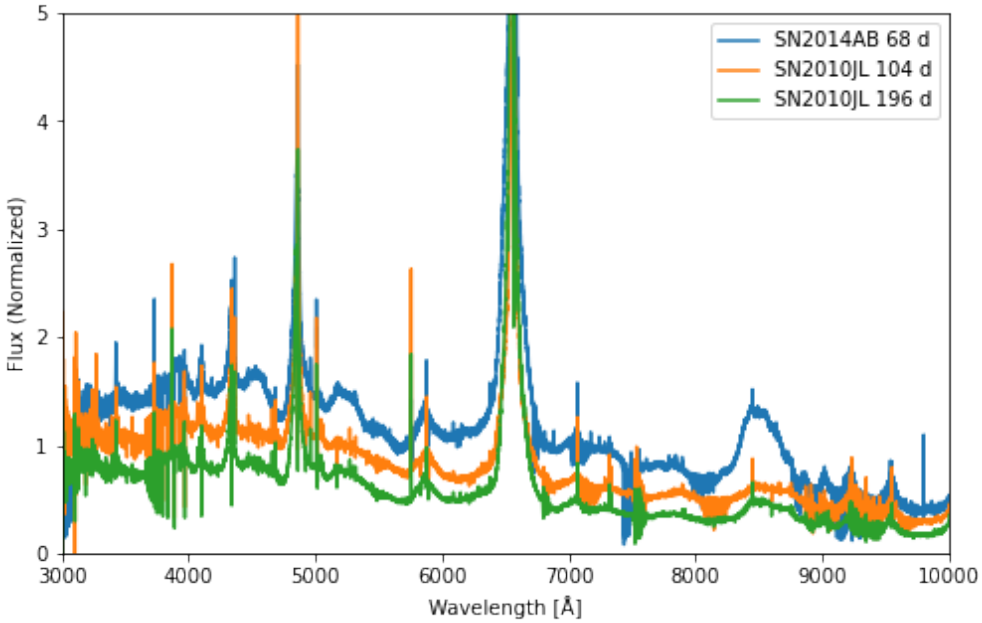

Figure 6.2: Comparison of the first epoch of SN 2014ab with two epochs of SN 2010jl. The date for SN 2014ab refers to days since the first WISE observation, whereas the dates for SN 2010jl refers to days past peak (Gall et al., 2014).

The spectrum of SN 2014ab has a strong Calcium line (around 8500 Å), which is not present in that of SN 2010jl until much later epochs. As calcium is formed in the layers within the ejecta, this is most likely due to the fact that the photosphere of SN 2014ab has been receding faster than for SN 2010jl, which likely had a more massive CSM (Gall et al., 2014). If the 104 d 2010jl spectrum matches the 68 d 2014ab spectrum, it means that the peak time of SN 2014ab was 32 days before discovery, with the explosion date most likely around 40 days before this point. This would depend on whether SN 2014ab has a slowly declining or fast declining LC (Nyholm et al., 2020).

In addition to comparing the full spectra, I also examined individual spectral emission lines. An example of this can be seen in Fig. 6.3 with Hα.

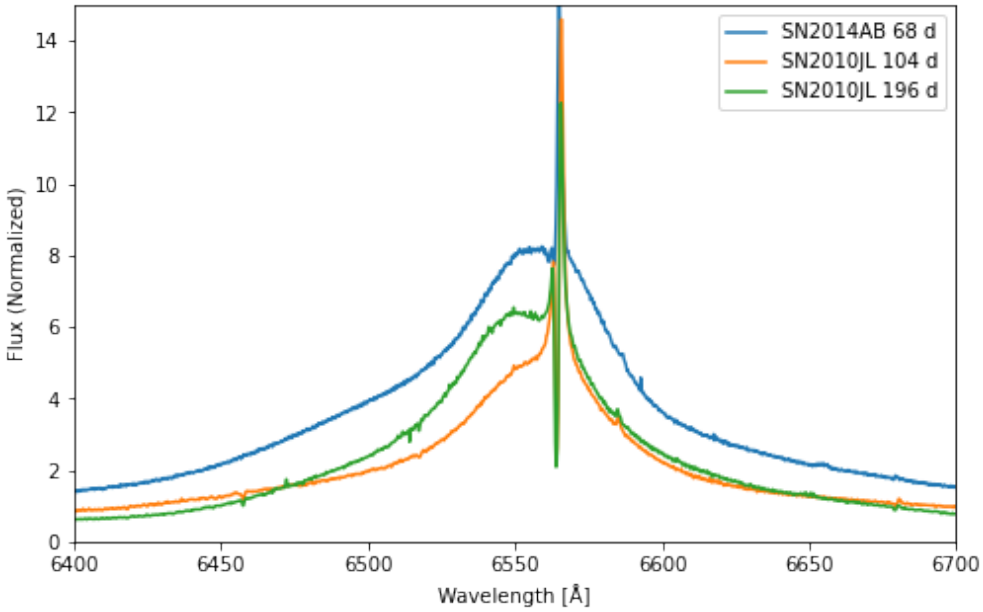

Figure 6.3: Comparison of Hα for the first epoch of SN 2014ab and two epochs of SN 2010jl. The date for SN 2014ab refers to days since the first WISE observation, whereas the dates for SN 2010jl refers to days past peak (Gall et al., 2014).

The blueshift for SN 2014ab at 68 d is not as large as that for SN 2010jl at 196 d, but more comparable to the blueshift of SN 2010jl at 104 d. However, the peak is more pronounced for SN 2010ab than for SN 2010jl at 104 d. The shape of this line is very dependent on the CSM, the CDS, how much dust forms, how much hydrogen is present etc. Thus, determining the epoch through comparison of the hydrogen line profiles may not be possible.

6.3.2 Extinction

Now I compare the extinction found from the spectral lines with that of SN 2010jl (Gall et al., 2014) and SN 2017hcc (Smith and Andrews, 2020), seen in Fig. 6.4 and 6.5.

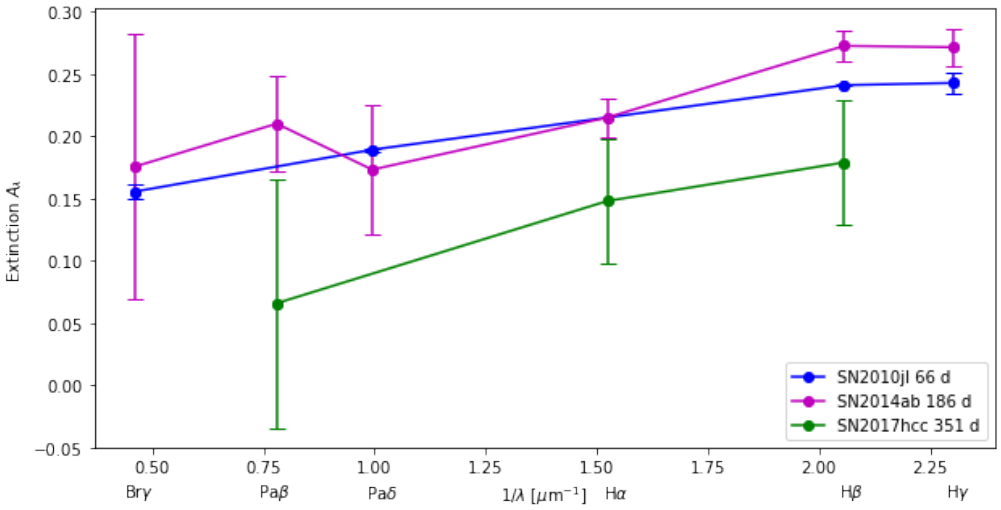

Figure 6.4: Comparison of the extinction values of SN 2014ab, SN 2010jl and SN 2017hcc. The date for SN 2014ab refers to days since the first WISE observation, the dates for SN 2010jl refers to days past peak (Gall et al., 2014) and the date for SN 2017hcc refers to days past explosion (Smith and Andrews, 2020).

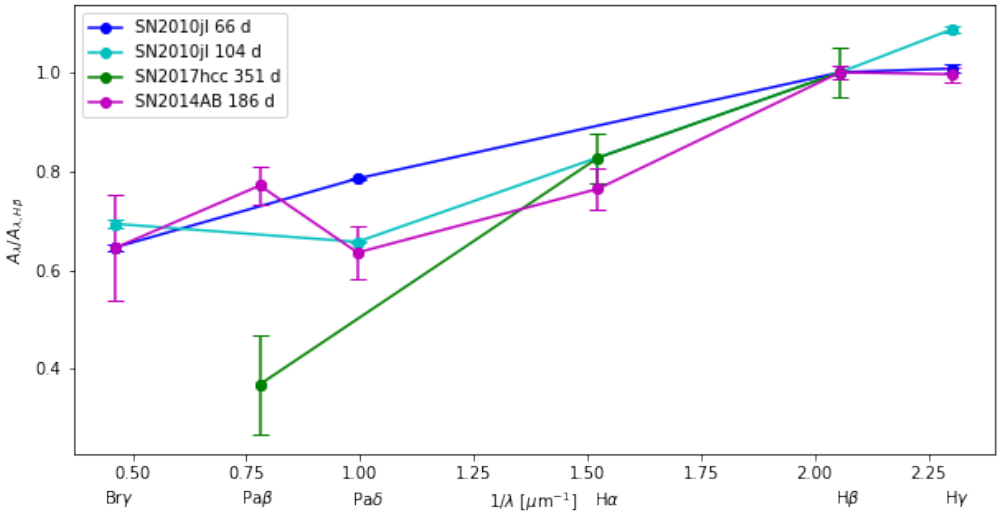

Figure 6.5: Comparison of the slope of the extinction curve of SN 2014ab, SN 2010jl and SN 2017hcc. Here all extinction values have been normalized to those of Hβ.

From Fig. 6.4 we can see that the values I found in the last epoch, 186 d, matches the values found in SN 2010jl at the early epoch 66 d. They are however slightly larger than those found in SN 2017hcc. This is especially evident for Paβ, however this is noted in Smith and Andrews, 2020: 'most of the extinction in Paβ occurs at the higher velocities'. Fig. 6.5 shows the extinction values normalized to Hβ. Here we see that the slope of the extinction curve is better represented by SN 2010jl 104 d and that the slope of 2017hcc (between Hα and Hβ) matches that found from SN 2014ab.
All three SNe have similar slopes to their extinction curves. Both SN 2010jl and SN 2017hcc had inferred R_V values larger than the average MW dust composition (with both having values of $R_V \sim 6$), which is in agreement with those found for SN 2014ab.

6.4 Previous Work on SN 2014ab

In the following I will discuss the cause of the differing results between this thesis and those found by Moriya et al., 2020. Secondly I will discuss why their conclusions are in disagreement with my findings.

Moriya et al., 2020 examined Hα and found that the centroid of the broad emission line had been blueshifted by 500 km s^{-1}, twice as large as that found by my inspection of the intermediate velocity component, which yielded a blueshift of around 250 km s^{-1}. Moriya et al., 2020 concluded that this blueshift is not time or wavelength dependent, however my results (see section 6.1) show that this blueshift is indeed time dependent, with all examined lines yielding increasing blueshifts for later epochs.
As Moriya et al., 2020 concluded that there were no signs of dust from inspection of this blueshift they never examined the extinction of the lines and thus have no extinction values that I can compare. It should be mentioned as well that whereas I have focused on the intermediate velocity component of the lines, which is where we expect to see ongoing dust formation, Moriya et al., 2020 focused on the broad component, which might explain their different results.

Moriya et al., 2020 examined the SEDs of SN 2014ab, using different photometric bands, by fitting these with a BB (see Fig. 6.6). However, only a single BB was used up to 140

days. For the last few epochs an extra BB was included, but not a modified BB as I have used in section 6.3. This means that even though a NIR excess was observed by Moriya et al., 2020, no dust mass was inferred from these fits.

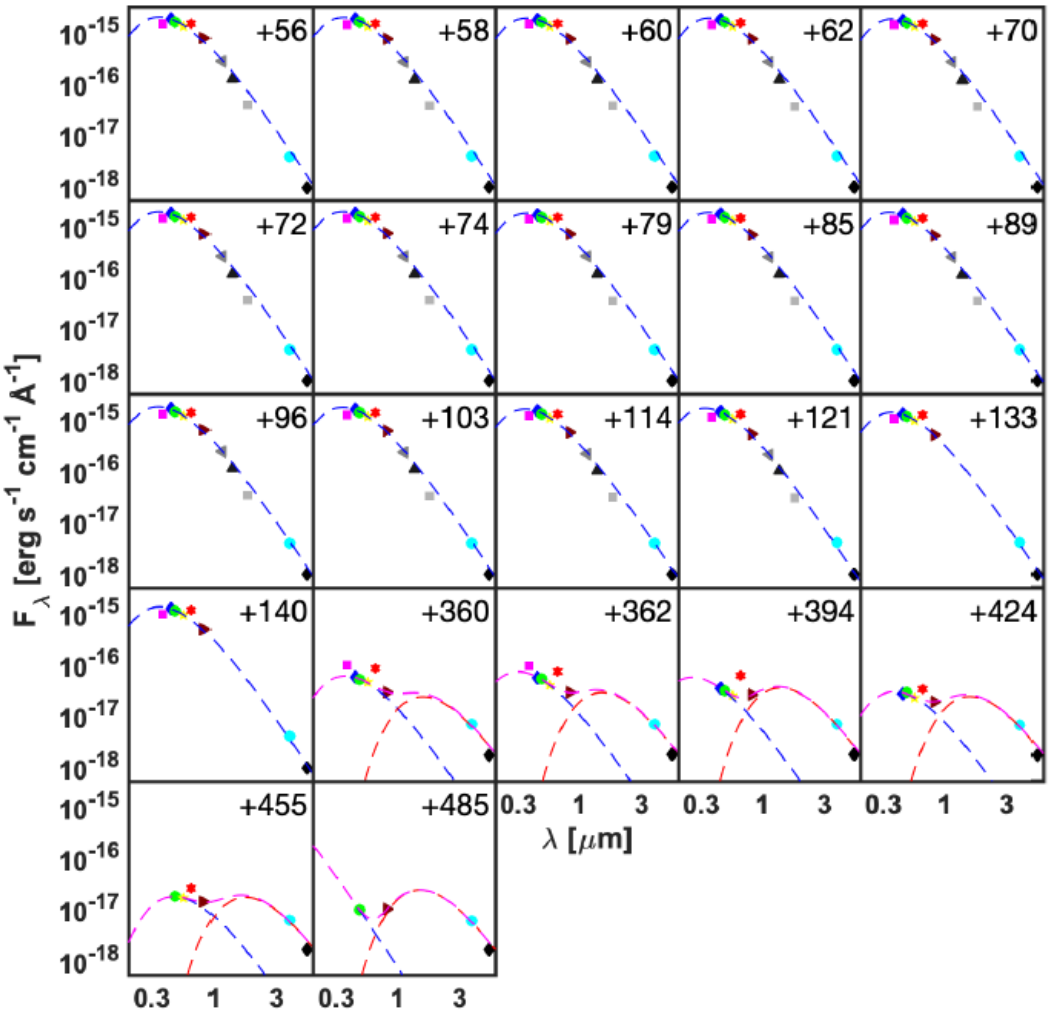

Figure 6.6: SEDs of SN 2014ab constructed by Moriya et al., 2020. From +56 d to +140 d the SEDs are fitted with a single BB, from +360 d to +485 the SEDs exhibit an excess of flux and are fitted with a two-component BB function.

So due to the fact that no evolution of the spectral lines was observed, Moriya et al., 2020 concluded that this IR excess wasn't the result of newly formed dust.
The overall blueshift of the broad emission lines is instead explained by the acceleration of the unshocked CSM by precursor photons. Further it is suggested that the blueshift possibly is affected by the radiation transfer effect in addition to this acceleration.
The observed IR excess, which points to the presence of dust in SN 2014ab, is concluded to not being the result of dust formed in the CDS, but instead due to pre-existing dust in the dense CSM heated by the SN shock or radiation. Moriya et al., 2020 further concludes that the component found to be associated with dust, appearing at 360 d in Fig. 6.6, is not present at early epochs. My analysis however shows that the dust component of the composite model is present already at 68 d, see Fig. 5.4a and 5.4b.

As discussed in section 6.1, this IR excess cannot be due to pre-existing dust as we then wouldn't see the blueshifted asymmetry observed in the line profiles. However what about the theory that it is a result of the acceleration of the unshocked CSM? If that was the case, then the blueshift would not persist to later epochs when the SN seizes to expand. This might still be happening at $\sim$ 200 d which is the latest epoch observed here, but that would not explain the wavelength dependence of the measured extinction. However more analysis of later epochs might be necessary to completely rule out this option.

Chapter 7

Conclusion

Current theories for dust formation are in disagreement with the amount of dust observed in various environments. One of the suggested sources of dust are CCSNe due to their short lifetimes and large production of metals. In this thesis I have examined the early dust formation in SN 2014ab and added to the growing observational evidence that dust is forming at early epochs in type IIn CCSNe.

I presented my analysis of VLT/X-shooter spectra spanning 5 epochs. From analysis of prominent emission lines I quantify the extinction from dust and find that it is both time and wavelength dependent, which points to ongoing dust formation. From a composite model of the full spectra I show that the IR excess emission is present in all epochs, and find values for the dust temperature, $T_{\rm dust} \sim 1500$ K, and dust mass, $M_{\rm dust} \sim 2.5 \cdot 10^4 M_{\odot}$ assuming graphite grains with a grain size of 0.1 micron. Assuming silicate grains, the dust temperature is slightly higher, $T_{\rm dust} \sim 1500$ K, and the dust mass is about a factor 10 larger than when assuming graphite grains.

I conclude that these signatures are due to ongoing dust formation as pre-existing dust would not be able to yield the wavelength dependency of the blueshift. The grain species and size is estimated by the two component fit and by fitting the extinction curve with standard extinction laws. The composite model favored grain sizes of 0.1 μm over those of 1 μm, however, the inferred $R_{\rm V}$ from fitting the extinction curve indicates a bigger fraction of large grains than for the average MW grain distribution.

Finally, the results are compared to those of SN 2010jl (Gall et al., 2014) and SN 2017hcc (Smith and Andrews, 2020), yielding similar results, though dust is forming at later epochs in SN 2014ab.

Chapter 8

Outlook

In this last chapter I discuss some possibilities for further research on SN 2014ab.

In this thesis I have focused only on the X-shooter spectra of SN 2014ab. However, as explained in chapter 3, a wide variety of data was taken over a larger time span. It would be interesting to examine e.g. the WISE data, to get better constraints on the NIR part of the composite model, or to examine the photometric data at later epochs to see how the SN evolves later on. If the blueshift persists to epochs later than the ones examined here, it would confirm that the blueshift stems from dust formation and not radiative acceleration, as this would disappear at later epochs.
In my thesis, this blueshift has been found by focusing purely on the intermediate velocity component of the spectral lines. However, this means that I have assumed what the range of this intermediate component is. Instead one could fit the whole spectral line with a composite model with one part for each component (narrow, intermediate and broad). This would give us a better estimate of the continuum level and a better understanding of the line profile.

It would be interesting as well to compare the spectra of SN 2014ab with more type IIn SNe with known explosion dates, so that we could be able to determine the actual age of each epoch. That would also enable us to give a more accurate picture of how early the dust is forming. This could also be helped by examining the LC of SN 2014ab and comparing it to the work done by Nyholm et al., 2020. By examining how slowly

or fast the LC is declining, we can determine the time it took to rise to peak value and thereby how many days passed from explosion till peak date.

For simplicity, the composite model for the whole spectra (section 4.4) took into account single grain sizes for one specific dust species. However, in reality the formed dust would likely be a composition of multiple species and distribution of sizes. One could implement a distribution of dust sizes in the model to get a more accurate image of the sizes of dust grains formed. This was for instance done by Gall et al., 2014 for SN 2010jl.

Finally, one could also fit the extinction curve with a model describing a distribution of dust types. However, with the amount of data available, that might be outside of what is reasonable. Instead, one could use a dust model such as DAMOCLES (Bevan and Barlow, 2016) to fit single emission lines with dust models. This is for instance done for SN 2010jl (Bevan et al., 2020).

Bibliography

Bevan, A. and M.J. Barlow (2016). "Modelling supernova line profile asymmetries to determine ejecta dust masses: SN 1987A from days 714 to 3604". In: *Monthly Notices of the Royal Astronomical Society* 456.2, pp. 1269–1293.

Bevan, A.M. et al. (2020). "Disentangling Dust Components in SN 2010jl: The First 1400 Days". In: *The Astrophysical Journal* 894.2, p. 111.

Bianchi, Simone and Raffaella Schneider (2007). "Dust formation and survival in supernova ejecta". In: *Monthly Notices of the Royal Astronomical Society* 378.3, pp. 973–982.

Cardelli, J.A., G.C. Clayton, and J.S. Mathis (1989). "The relationship between infrared, optical, and ultraviolet extinction". In: *The Astrophysical Journal* 345, pp. 245–256.

Dwek, E. et al. (2021). "The infrared echo of SN2010jl and its implications for shock breakout characteristics". In: *arXiv preprint arXiv:2106.06531*.

Fitzpatrick, E.L. and D. Massa (2005). "An analysis of the shapes of ultraviolet extinction curves. IV. extinction without standards". In: *The Astronomical Journal* 130.3, p. 1127.

Freedman, R. (2014). *Universe*. New York: W.H. Freeman and Company, a Macmillan Higher Education Company. ISBN: 1319042384.

Gall, C. and J. Hjorth (2018). "Maximally dusty star-forming galaxies: supernova dust production and recycling in local group and high-redshift galaxies". In: *The Astrophysical Journal* 868.1, p. 62.

Gall, C., J. Hjorth, and A.C. Andersen (2011). "Production of dust by massive stars at high redshift". In: *The Astronomy and Astrophysics Review* 19.1, p. 43.

Gall, C. et al. (2014). "Rapid formation of large dust grains in the luminous supernova 2010jl". In: *Nature* 511.7509, pp. 326–329.

Henning, Thomas (2010). "Cosmic silicates". In: *Annual Review of Astronomy and Astrophysics* 48, pp. 21–46.

Jiang, N. et al. (2019). "Infrared Echo and Late-stage Rebrightening of Nuclear Transient Ps1-10adi: Exploring the Torus with Tidal Disruption Events in Active Galactic Nuclei". In: *The Astrophysical Journal* 871.1, p. 15.

Li, Aigen and BT Draine (2001). "Infrared emission from interstellar dust. II. The diffuse interstellar medium". In: *The Astrophysical Journal* 554.2, p. 778.

Mathis, John S, William Rumpl, and Kenneth H Nordsieck (1977). "The size distribution of interstellar grains". In: *The Astrophysical Journal* 217, pp. 425–433.

Módolo, M., L.N.F. Guimarães, and R.R. Rosa (2015). "An expert supernova spectral classification using artificial neural networks". In: *J Comp Int* 6.2, pp. 81–90.

Moriya, T.J. et al. (2020). "The Carnegie Supernova Project II-Observations of SN 2014ab possibly revealing a 2010jl-like SN IIn with pre-existing dust". In: *Astronomy & Astrophysics* 641, A148.

Nozawa, Takaya et al. (2003). "Dust in the early universe: dust formation in the ejecta of population III supernovae". In: *The Astrophysical Journal* 598.2, p. 785.

Nyholm, A. et al. (2020). "Type IIn supernova light-curve properties measured from an untargeted survey sample". In: *Astronomy & Astrophysics* 637, A73.

Rouleau, Francois and PG Martin (1991). "Shape and clustering effects on the optical properties of amorphous carbon". In: *The Astrophysical Journal* 377, pp. 526–540.

Sarangi, A., M. Matsuura, and E.R. Micelotta (2018). "Dust in supernovae and supernova remnants I: formation scenarios". In: *Space Science Reviews* 214.3, pp. 1–48.

Sluder, A. and M. H. Milosavljević M.and Montgomery (2018). "Molecular nucleation theory of dust formation in core-collapse supernovae applied to SN 1987A". In: *Monthly Notices of the Royal Astronomical Society* 480.4, pp. 5580–5624.

Smith, N. (2016). "Interacting supernovae: types IIn and Ibn". In: *arXiv preprint arXiv:1612.02006*.

Smith, N (2017). "Luminous blue variables and the fates of very massive stars". In: *Philosophical Transactions of the Royal Society A: Mathematical, Physical and Engineering Sciences* 375.2105, p. 20160268.

Smith, N. and J.E. Andrews (2020). "High-resolution spectroscopy of SN 2017hcc and its blueshifted line profiles from post-shock dust formation". In: *Monthly Notices of the Royal Astronomical Society* 499.3, pp. 3544–3562.

Todini, Paolo and Andrea Ferrara (2001). "Dust formation in primordial Type II supernovae". In: *Monthly Notices of the Royal Astronomical Society* 325.2, pp. 726–736.

Wakelam, Valentine et al. (2017). "H2 formation on interstellar dust grains: The viewpoints of theory, experiments, models and observations". In: *Molecular Astrophysics* 9, pp. 1–36.

Appendix A

Supplementary results

	FWHM [km s^{-1}]				
Line	68 d	100 d	160 d	166 d	186 d
Brγ	1825.6±185.3	1614.9±99.5	1626.6±108.1	1794.8±121.6	1538.0±87.8
Paβ	2734.3±201.4	2829.7±275.5	2937.5±141.9	3008.6±113.5	2960.8±111.5
Paδ	2973.8±201.4	3556.8±275.5	2850.7±141.9	2650.6±113.5	2732.4±111.5
Hα	1607.8±12.2	1717.8±15.3	1684.5±14.5	1674.3±14.2	1607.4±14.4
Hβ	2043.5±73.8	1934.0±61.2	1765.4±35.3	1771.7±42.8	1711.7±32.2
Hγ	1682.4±45.9	1588.1±38.8	1455.3±31.7	1488.1±31.0	1411.9±31.0
Hδ	1958.9±140.3	1712.9±88.2	1789.3±88.7	1450.4±62.4	1606.4±66.3

Table A.1: FWHM of each spectral line, found from the Lorentzian fits to the intermediate component.

Composite model				
Epoch	T_{SN} [K]	$R_{SN} \cdot 10^{15}$ [cm]	T_{dust} [K]	$M_{dust} \cdot 10^{-4}$ [$M_{\odot}$]
68 d	7000.00±3.39	2.29±0.003	1591.29±67.09	1.00±0.59
100 d	7179.07±3.89	2.09±0.003	1565.81±79.44	0.98±0.24
160 d	7063.38±4.32	1.90±0.003	1639.27±11.82	4.66±0.20
166 d	7091.06±4.01	1.70±0.002	1746.86±6.96	4.00±0.09
186 d	6991.38±4.49	1.50±0.002	1717.99±5.40	4.73±0.09

Table A.2: Evolution of fit parameters for the composite model, assuming silicate 1 μm.

Composite model				
Epoch	T_{SN} [K]	$R_{SN} \cdot 10^{15}$ [cm]	T_{dust} [K]	$M_{dust} \cdot 10^{-4}$ [$M_{\odot}$]
68 d	7001.30±3.29	2.29±0.002	1488.98±46.77	0.99±0.13
100 d	7196.60±3.77	2.08±0.002	1500.00±914.28	1.00±0.23
160 d	7074.08±4.48	1.90±0.003	1776.35±12.99	1.38±0.06
166 d	7110.73±4.18	1.68±0.002	1893.90±7.68	1.21±0.03
186 d	7012.73±4.67	1.49±0.002	1849.86±5.95	1.47±0.03

Table A.3: Evolution of fit parameters for the composite model, assuming graphite 1 μm.

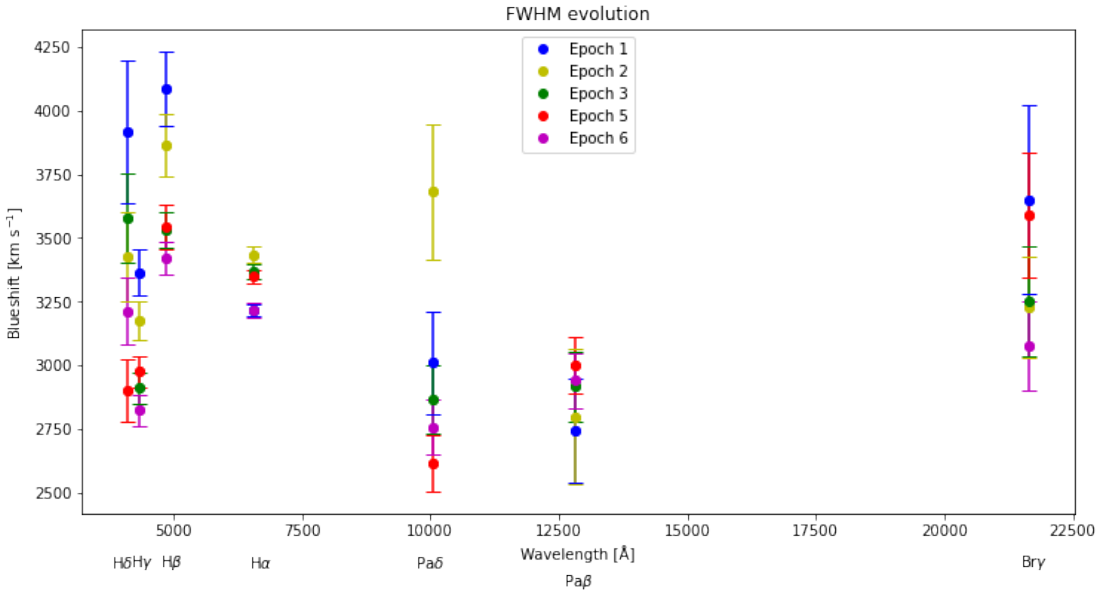

Figure A.1: FWHM of the Lorentzian fits of each epoch.

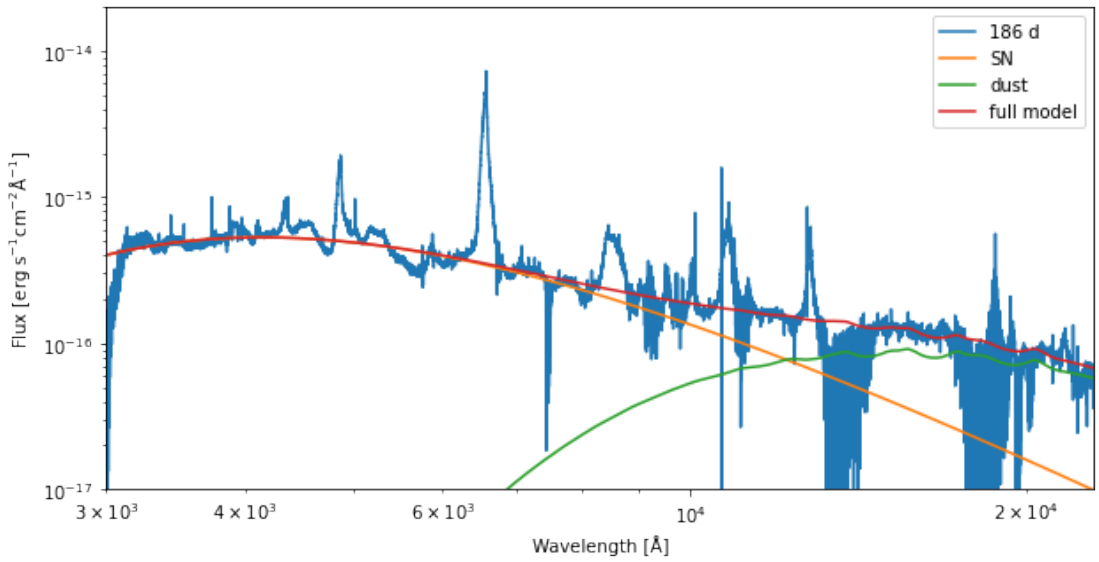

Figure A.2: Composite model for the last epoch, assuming graphite 1 μm.

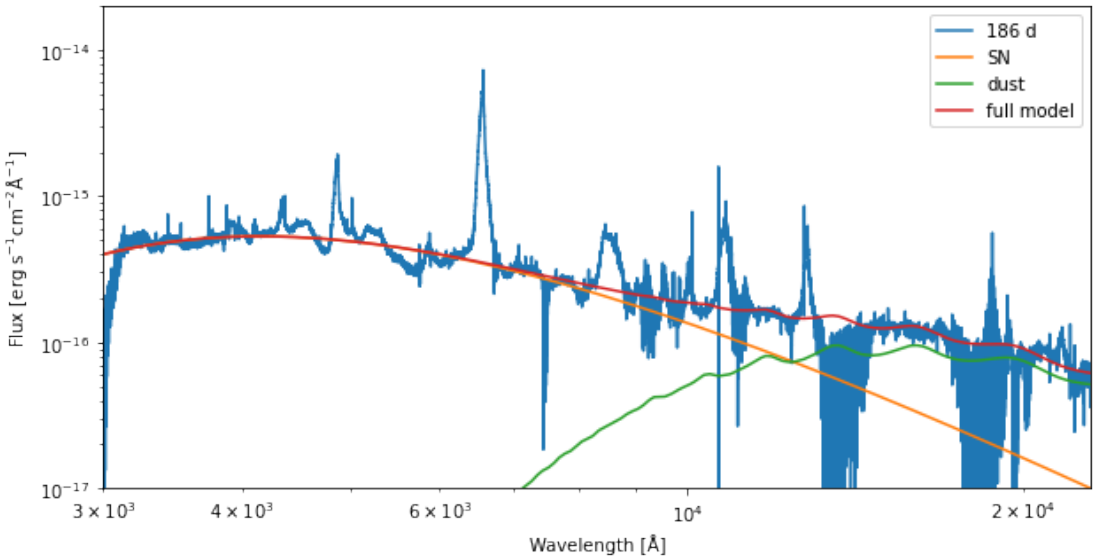

Figure A.3: Composite model for the last epoch, assuming silicate 1 μm.

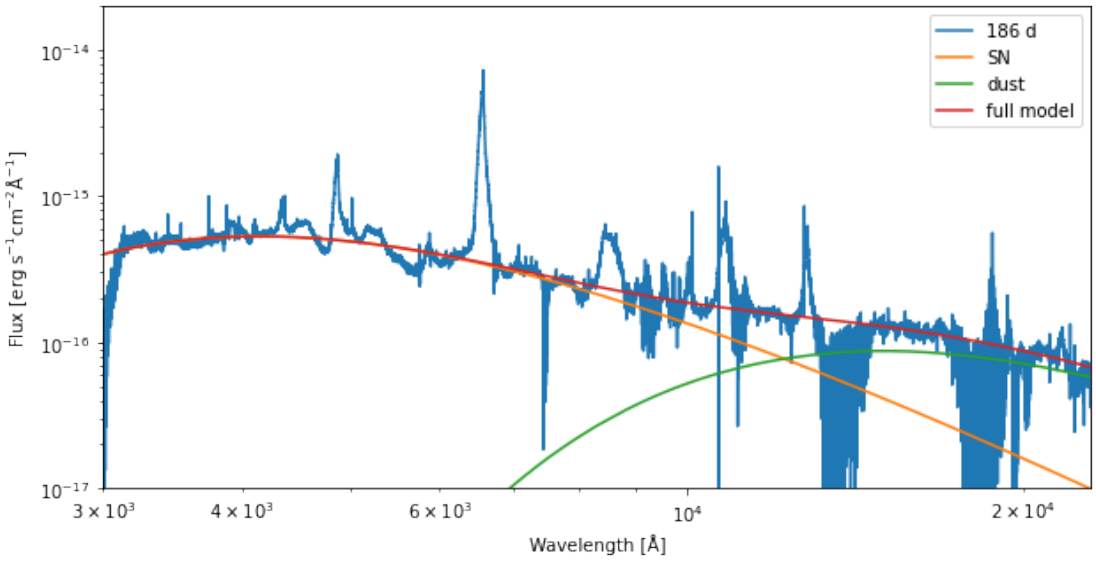

Figure A.4: Composite model for the last epoch, assuming silicate 0.1 μm.